Article

Cell Systems

A Map of Human Mitochondrial Protein Interactions Linked to Neurodegeneration Reveals New Mechanisms of Redox Homeostasis and NF-κB Signaling

Graphical Abstract

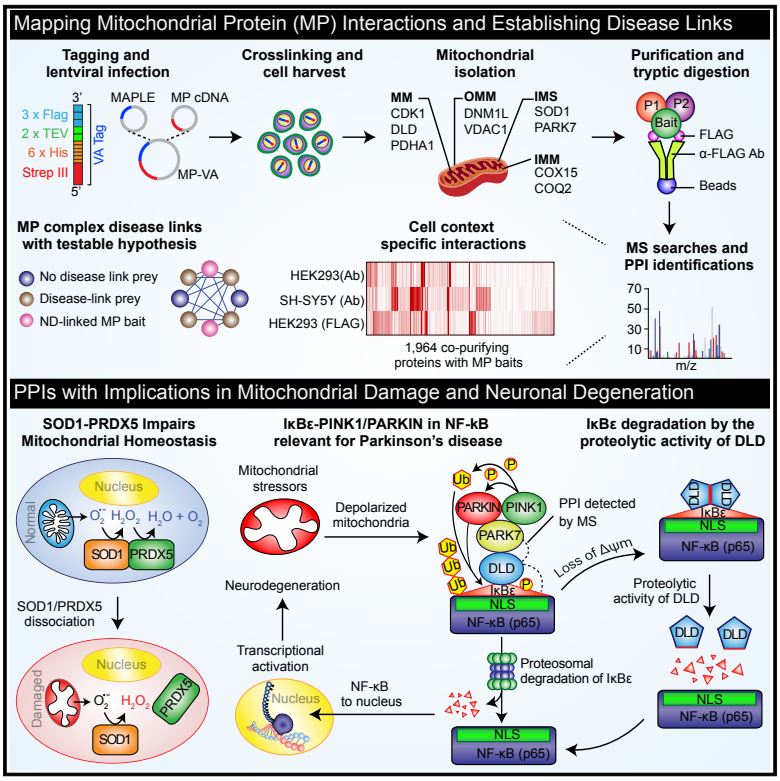

Highlights

- Interactions mapped for mitochondrial proteins involved in neurodegeneration
- Interaction partners in mitochondrial network linked to autism
- IκBε is degraded by the proteolytic activity of its binding partner, DLD
- PD-relevant PINK1-PARKIN complex activates NF-κB via IκBε

Authors

Ramy H. Malty, Hiroyuki Aoki, Ashwani Kumar, ..., Ken Nakamura, John Parkinson, Mohan Babu

Correspondence

mohan.babu@uregina.ca

In Brief

Mitochondrial protein (MP) dysfunction has long been linked to neurodegenerative disorders (NDs), yet the molecular mechanisms underlying NDs have been obfuscated by the limited characterization of protein-protein interactions (PPIs) governing mitochondrial function. Through mass spectrometry analysis of affinity-purified mitochondrial fractions isolated from epitope-tagged human ND-linked MPs, Malty et al. report a high-confidence MP network with PPIs relevant for neurological function and reveal new mechanisms for MPs in redox homeostasis (SOD1-PRDX5) and NF-κB activation (IκBε- DLD or PINK1/PARKIN).

Malty et al., 2017, Cell Systems 5, 564–577
December 27, 2017
https://doi.org/10.1016/j.cels.2017.10.010

CellPress

Cell Systems
Article

A Map of Human Mitochondrial Protein Interactions Linked to Neurodegeneration Reveals New Mechanisms of Redox Homeostasis and NF-κB Signaling

Ramy H. Malty,[1] Hiroyuki Aoki,[1] Ashwani Kumar,[2] Sadhna Phanse,[1] Shahreen Amin,[1] Qingzhou Zhang,[1] Zoran Minic,[1] Florian Goebels,[3] Gabriel Musso,[4] Zhuoran Wu,[1] Hosam Abou-tok,[1] Michael Meyer,[5] Viktor Deineko,[1] Sandy Kassir,[1] Vishaldeep Sidhu,[1] Matthew Jessulat,[1] Nichollas E. Scott,[6] Xuejian Xiong,[7] James Vlasblom,[1] Bhanu Prasad,[8] Leonard J. Foster,[6] Tiziana Alberio,[9] Barbara Garavaglia,[10] Haiyuan Yu,[5] Gary D. Bader,[3] Ken Nakamura,[11] John Parkinson,[7] and Mohan Babu[1,12,*]

[1]Department of Biochemistry, University of Regina, Regina, SK S4S 0A2, Canada
[2]Department of Computer Science, University of Regina, Regina, SK S4S 0A2, Canada
[3]The Donnelly Centre, University of Toronto, Toronto, ON M5S 3E1, Canada
[4]Department of Medicine, Harvard Medical School and Cardiovascular Division, Brigham and Women's Hospital, Boston, MA 02115, USA
[5]Department of Biological Statistics and Computational Biology, Cornell University, Ithaca, NY 14853, USA
[6]Department of Biochemistry and Molecular Biology, University of British Columbia, Vancouver, BC V6T 1Z3, Canada
[7]Hospital for Sick Children, 21-9830 PGCRL, 686 Bay Street, Toronto, ON M5G 0A4, Canada
[8]Department of Medicine, Regina Qu'Appelle Health Region, Regina, SK S4P 0W5, Canada
[9]Department of Science and High Technology, Center of Neuroscience, University of Insubria, Via Alberto da Giussano 12, Busto Arsizio I-21052, Italy
[10]Molecular Neurogenetics Unit, IRCCS Foundation C. Besta Neurological Institute, via L. Temolo, 4, 20126 Milan, Italy
[11]Gladstone Institute of Neurological Disease, San Francisco, CA 94158, USA
[12]Lead Contact
*Correspondence: mohan.babu@uregina.ca
https://doi.org/10.1016/j.cels.2017.10.010

SUMMARY

Mitochondrial protein (MP) dysfunction has been linked to neurodegenerative disorders (NDs); however, the discovery of the molecular mechanisms underlying NDs has been impeded by the limited characterization of interactions governing MP function. Here, using mass spectrometry (MS)-based analysis of 210 affinity-purified mitochondrial (mt) fractions isolated from 27 epitope-tagged human ND-linked MPs in HEK293 cells, we report a high-confidence MP network including 1,964 interactions among 772 proteins (>90% previously unreported). Nearly three-fourths of these interactions were confirmed in mouse brain and multiple human differentiated neuronal cell lines by primary antibody immunoprecipitation and MS, with many linked to NDs and autism. We show that the SOD1-PRDX5 interaction, critical for mt redox homeostasis, can be perturbed by amyotrophic lateral sclerosis-linked *SOD1* allelic variants and establish a functional role for ND-linked factors coupled with IκBε in NF-κB activation. Our results identify mechanisms for ND-linked MPs and expand the human mt interaction landscape.

INTRODUCTION

The importance of mitochondria (mt) is underscored by a number of human diseases associated with mt dysfunction (Nunnari and Suomalainen, 2012), including neurodegenerative disorders (NDs) such as Parkinson's disease (PD) and amyotrophic lateral sclerosis (ALS). Large-scale proteomic analyses have advanced our knowledge of the composition of the mt proteome in mouse and human (Calvo et al., 2016; Pagliarini et al., 2008), allowing identification of mt disease gene candidates and gene-disease associations for MPs (Floyd et al., 2016; Malty et al., 2015). Active mechanisms coordinate the assembly of an estimated 1,500 nuclear- and 13 mt-encoded proteins into macromolecular complexes (Malty et al., 2015). Yet, little is known about the biochemical organization of human mitochondrial protein (MP) complexes, and how human MPs interact within mt, between mt, and with proteins outside of the mt to contribute to the pathophysiology of mt diseases. These gaps impede the development of effective therapeutics for human mt disorders.

Since most cellular processes are mediated by macromolecular assemblies, the systematic identification of mt protein-protein interactions (mtPPIs) and the subunit composition of complexes can provide insights into protein function and decipher the molecular basis of disease. As a result, characterization of disease-linked PPI networks is being exploited as a means of therapeutic target identification and to develop translational clinical applications (Barabasi et al., 2011). While such human PPIs can be detected by several experimental means, affinity purification coupled with mass spectrometry (AP/MS) is well suited for large-scale isolation and characterization of protein complexes in many evolutionarily diverse organisms, including humans (reviewed in Huttlin et al., 2017).

Despite the large and near-comprehensive human interaction networks generated to date (Havugimana et al., 2012; Hein et al., 2015; Huttlin et al., 2017), very few MPs have been used as baits in previous studies, with interactions largely reported

from human whole-cell, nuclear, or cytosolic extracts. As a result, mt interactions have been undersampled. Recent efforts to map a condition-specific human mtPPI network in mammalian cells have been successful in assigning functions for some previously uncharacterized MPs (Floyd et al., 2016), but inherent technical challenges associated with organelle purification have limited the coverage of the human mtPPI network and cell-type specific interactions in mammalian cells, particularly among ND-linked proteins. Here, to overcome these problems, we report an AP/MS framework, with experimental parameters optimized to systematically tag and affinity purify the mt fraction isolated from 27 well-annotated ND-linked MPs expressed in HEK293 cells, identifying their interaction partners by precision MS.

The assembled PPI network encompasses putative hetero- and multi-meric MP complexes, including several not previously reported. Since the tagged MPs are linked with NDs, we compared the PPIs of these proteins in HEK293 cells with those identified from differentiated SH-SY5Y neuronal cells and identified prey proteins associated with autism spectrum disorders (ASD). Finally, we show the biological significance of selected connections between peroxiredoxin 5 (PRDX5) and ALS-linked CuZn-superoxide dismutase (SOD1), as well as between nuclear factor-κB (NF-κB) inhibitor ε (IκBε) and ND-linked proteins (DLD or PINK1, PARKIN) in mouse N9 microglial cells and human PD patient (*PINK1* or *PARKIN* mutations) fibroblasts. These interactions have direct implications for our understanding of cellular damage to mt and the role of ND-related proteins in this process.

RESULTS

AP/MS Screen for MPs

To facilitate a proteome-wide mt interaction screen in human cells, we chose a set of 27 nuclear-encoded human MPs associated with various NDs that function broadly in distinct mt processes and are localized to the mt matrix, inner or outer membrane, intermembrane space, and to both the mt and other cellular organelles (Table S1). Since hydrophobic MP complexes are difficult to purify, we developed an alternate affinity isolation procedure for MPs. This involved introducing the triple (FLAG-HIS-STREP) versatile affinity (VA) epitope tag at the C terminus (mt localization typically requires an amino-terminal signal peptide for MP import) by creating HEK293 cell lines stably expressing the VA-tagged human MPs by lentiviral transduction (Figure 1A). Subsequently, mt were isolated with high yield from cultured HEK293 cells expressing tagged MPs using cross-linking and buffers containing a mild, non-denaturing detergent for mt membrane protein solubilization.

Prior to AP/MS, several pilot experiments were conducted to optimize conditions for probing PPIs for each of the targeted MPs. Tagged MP expression was confirmed in the stably transduced HEK293 cells by immunoblotting using the anti-FLAG antibody (Ab; Figures 1B and S1A). To ensure that the C-terminal VA tag did not interfere with localization and protein function or expression, we examined the tagged MPs by immunofluorescence staining. As expected, cells expressing VA-tagged MPs showed co-localization with anti-FLAG Ab and MitoTracker, which selectively stains mt (Figure 1C). Consistent with this, cells expressing VA-tagged MPs also showed significantly ($p \leq 0.05$) increased activity of succinate dehydrogenase (an mt enzyme marker) and decreased activity of lactate dehydrogenase (a cytoplasmic enzyme) in mt versus cytosolic or total lysate fractions (Figure 1D). This finding was further confirmed by immunoblotting subcellular fractions with anti-FLAG Ab (Figure 1E).

Comparison of protein expression levels of VA-tagged MPs with corresponding endogenous proteins in HEK293 cells showed that tagged bait expression levels were present very close to or below endogenous levels (Figure 1F). Additional tests with single-step FLAG purification and chemical crosslinking with dithiobis succinimidyl propionate (DSP) showed increased bait recovery for MPs (Figure 1G). Since hydrophobic MPs are challenging to solubilize, we used a mild detergent extraction procedure adapted from our large-scale study of yeast membrane proteins (Babu et al., 2012). After evaluating ten detergents (Figure S1B), we selected digitonin (1% w/v) and purified each of the 27 targeted VA-tagged MPs with a chemical cross-linker, in at least three biological replicates, for a total of 210 single-step FLAG purifications (Table S1). The purified MP samples were then trypsinized and analyzed by Orbitrap MS.

Generating and Benchmarking mtPPIs

In total, 13 of the 27 VA-tagged bait MPs detected by MS in HEK293 cells exhibited high reproducibility ($r = 0.71$; Figure 2A) between biological replicate purifications, whereas the undetected bait proteins showed low expression by RNA-seq ($p = 8.6 \times 10^{-3}$; Figure 2B). As with the immunoblot analysis (Figure 1G), crosslinking favored capturing half (411 of 910, 45%) of the prey proteins from MS (Figure S1C), suggesting an effective means for identifying stable or transient PPIs. Where possible, we purified the same set of 13 recovered bait MPs in both HEK293 and differentiated SH-SY5Y neuronal cells (a human neuroblastoma model cell line for studying NDs), with protein-specific Abs, using immunoprecipitation (IP) and MS (Li et al., 2015). This allowed us to evaluate if the overexpression system used here may alter interaction dynamics in a neuronal context.

To define genuine associations, PPI data from the 13 FLAG-recovered MP purifications were filtered at a confidence threshold of 90% from MS. Interactions below the median normalized spectral abundance factor (NSAF) value observed in the wild-type (WT) HEK293 control purifications, as well as those PPI pairs not captured endogenously in the Ab datasets, were eliminated (Figure S1D). This resulted in a final network of 1,964 high-confidence associations (Table S1) encompassing 772 proteins (herein referred as the FLAG MP network). The vast majority of these PPIs (1,835, 93%) have not been reported previously (Figure 2C), reflecting the differences in methodology when surveying for MP interactions.

Several independent criteria supported the overall reliability and data quality of the MP associations. We found that the interacting MPs at >90% threshold from MS were significantly enriched ($p < 2.2 \times 10^{-16}$; Figure 2D) for literature-curated human mtPPIs (Table S2). Putative interaction partners are also more consistent in terms of the localization and shared Gene Ontology (GO) term function (Figure 2E) with respective bait MP, co-localization ($p = 1.8 \times 10^{-2}$) to the same mt compartment (Figure S1E), and higher ($p = 1.4 \times 10^{-18}$) functional coherence (average sematic similarity; Figure S1F) than previously published high-throughput (Havugimana et al., 2012; Huttlin et al., 2017; Wan

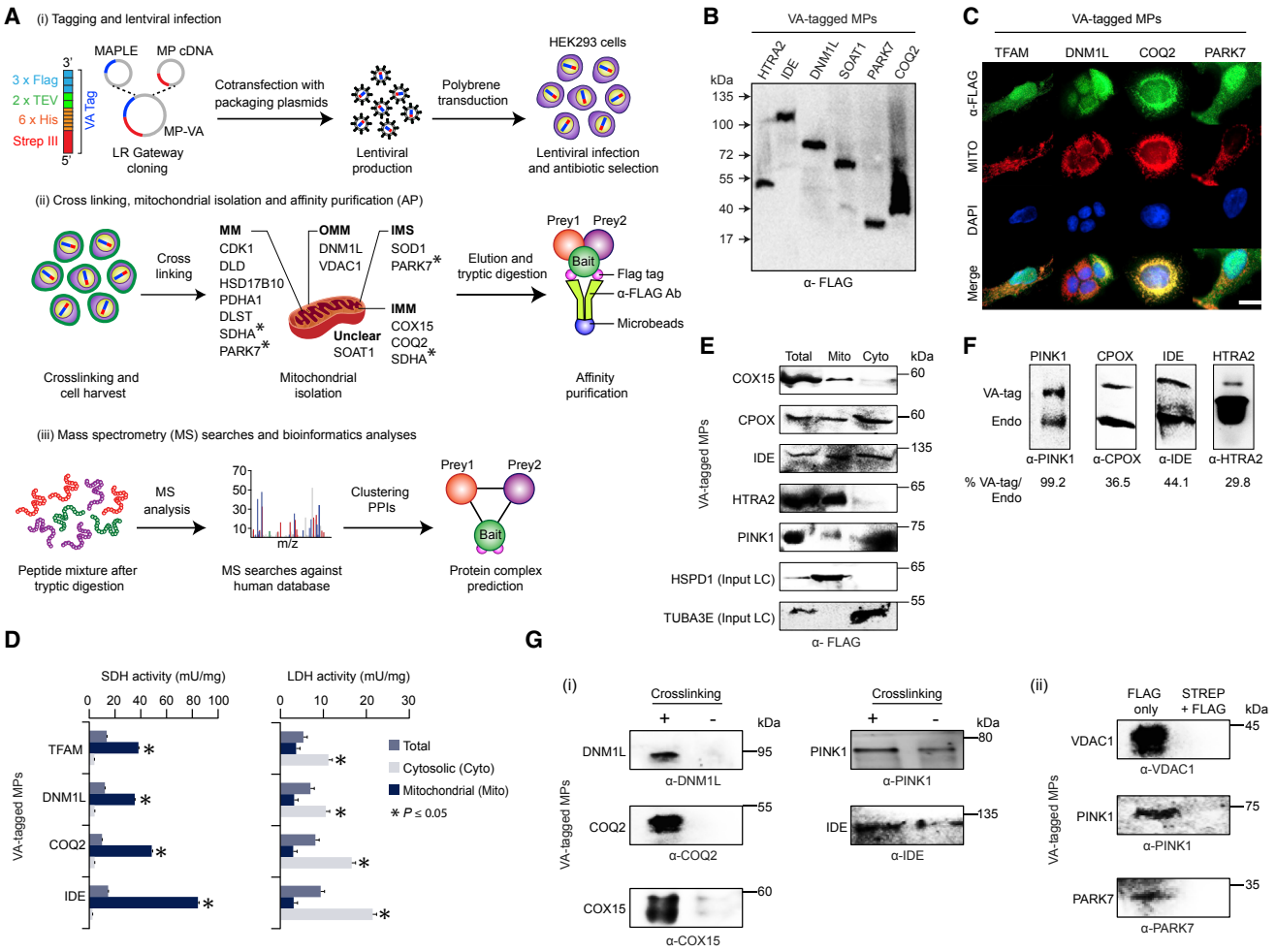

Figure 1. AP/MS Workflow and Characterization of VA-Tagged MPs in HEK293 Cells

(A) Lentivirus/cell-culture-based versatile affinity (VA) tagging of ND-linked MPs (i), followed by purification of mt fractions isolated from tagged proteins (bait MPs recovered from AP/MS shown; Table S1) coupled with MS (ii and iii). The resulting PPIs were clustered by coreMethod to predict protein complexes (iii). MAPLE, mammalian affinity purification and lentiviral expression; IMM/OMM, inner/outer mt membrane; MM, mt matrix; IMS, intermembrane space; unclear, unclear subcellular localization; and *dual localized.

(B) FLAG-epitope detection in VA-tagged MPs (see also Figure S1). Molecular mass markers (kDa) are indicated.

(C) Fluorescence micrographs of tagged MPs showing co-localization with anti-FLAG Ab (green) and mitotracker (red); DNA indicated by DAPI (blue). Scale bar, 10 μm.

(D and E) Succinate dehydrogenase (SDH) and lactate dehydrogenase (LDH) activities (n = 4, error bars are mean ± SD; *p value, Student's t test; D) as well as immunoblot (E) analyses of the indicated fractions from tagged MPs using FLAG Ab. The input from mt (HSPD1) or cytosolic (TUBA3E) marker used as loading control (LC).

(F) VA-tagged MP levels versus their endogenous (Endo) counterparts.

(G) Detection of VA-tagged MPs in HEK293 cells, with (+) or without (−) crosslinking (i), and after purifying crosslinked cells with single- (FLAG) or dual-step (Strep-Tactin [STREP] + FLAG) purifications (ii) using protein-specific Abs.

et al., 2015) or literature-curated interactors in BioGRID and CORUM. Among the binding partners of the MP baits, we observed an enrichment for 14-3-3 and canonical RNA-binding domains. These domains are associated with mt biogenesis, apoptosis, and stress response (Figure S1G; Table S2), supporting the notion that the interacting proteins are participating in mt processes.

To further assess if PPIs were erroneously identified due to exogenous expression, we compared the interacting partners from the FLAG MP network with the corresponding endogenous PPIs identified using protein-specific Abs in HEK293 and SH-SY5Y cells. We found that three-fourths (1,410, 72%; Figure 2F) of the total PPIs, encompassing 538 proteins from the FLAG MP network, were recapitulated in at least one of the Ab datasets. This is consistent with the accuracy seen with biological replicates of the same purification (Figure 2A).

While NSAF of the binding partner for MP baits in the FLAG MP network showed negative correlation ($r = -0.33$; Figure S2A) with protein abundance (Wang et al., 2012) due to the overcorrection of NSAF for protein length as previously reported (Ning et al.,

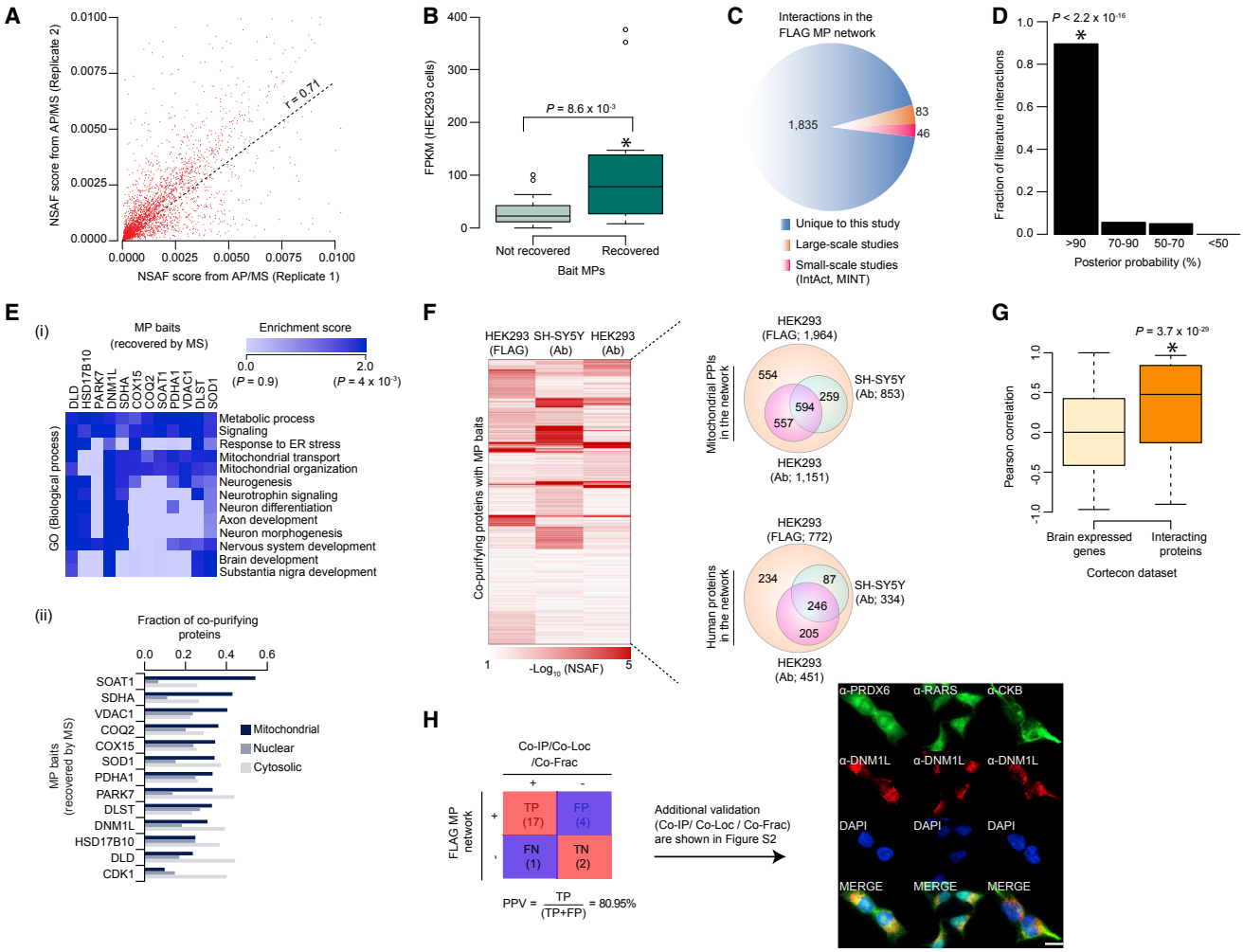

Figure 2. MP Interaction Data Quality

(A) Reproducibility of NSAF scores measured for each PPI pair in replicate AP/MS screens.

(B) mRNA expression levels from RNA-seq shown for tagged bait MPs that were recovered and not recovered in HEK293 cells from AP/MS; *p value, Fisher's exact test.

(C) MP interactions in the network compared with large- or small-scale studies (see Table S2).

(D) Comparison of mtPPIs at various MS probability thresholds to literature PPIs.

(E) Binding partners of the bait MPs with their: (i) Gene Ontology (GO) term enrichment for biological process (p value, Gene Set Enrichment Analysis), and (ii) distribution in nuclear, mt, and cytosol compartments.

(F) Heatmap showing NSAF scores ($-\log_{10}$ transformed) for mtPPI pairs using FLAG or protein-specific Ab in HEK293 or SH-SY5Y cells. Venn diagrams displaying the overlap of mtPPIs and human proteins among different cell lines and purification methods.

(G) Pearson correlation of expression profiles for interacting proteins in cortical neurons (see Table S3); *p value (D and G), Mann-Whitney-Wilcoxon test.

(H) PPIs confirmed by co-IP, co-fractionation (co-Frac; see Figure S2), and co-localization (co-Loc) in HEK293 cells using the indicated Abs (positive (+) or negative (−) PPI pairs tested are shown; PPV, positive prediction value); DNA visualized by DAPI (blue). Scale bar, 10 μm.

2012), we found interacting partners to be preferentially ($p = 2.1 \times 10^{-108}$) expressed in HEK293 and/or SH-SY5Y cells (Figure S2B) and showed positively correlated co-expression in cortical neurons (van de Leemput et al., 2014) and within human anatomical brain regions (Figures 2G and S2C; Table S3). The latter observation suggests a tendency toward coordinated expression of proteins interacting in a neuronal context. Finally, the biological relevance of the PPIs was validated by randomly selecting 24 PPI pairs from the FLAG MP network and confirming their associations using co-localization and biochemical assays. This verified the interactions of over three-fourths (17, 81%) of the MP pairs tested (Figures 2H and S2D–S2F; Table S2), consistent with the global validation using IP/MS in HEK293 and SH-SY5Y cells (Figure 2F).

Topological Properties of the FLAG MP Network and Relevance to Neurodegeneration

Since the topological features of a network determine the basic properties of its function and robustness (reviewed in Barabasi et al., 2011), we examined the behavior of the FLAG MP network

to determine how the binding partners of ND-linked MPs are connected to each other. Consistent with other human PPI networks (Havugimana et al., 2012; Huttlin et al., 2017), interactors in the FLAG MP network showed a power-law degree distribution, which is indicative of a scale-free network (reviewed in Barabasi et al., 2011). Half (53%, 410) of the proteins in the FLAG MP network had connectivity with two or more bait MPs (Figure S3A) and with fewer degrees of separation (Figure S3B). The network was also enriched ($p = 9.5 \times 10^{-3}$) for physical associations between proteins of mt and non-mt origin, as opposed to between mt constituents (Figure S3C), suggesting a tight integration of the mt with other cellular processes.

Examination of the FLAG MP network (Table S1) revealed several known PPIs involving components of the pyruvate dehydrogenase (PDH) complex; specifically, between PDHB (PDH E1 β subunit) and PDHA1 (PDH E1α subunit), which converts pyruvate into acetyl-CoA (Kanda et al., 2015). An interaction was also observed between the mt outer membrane channel (VDAC1) and inner membrane cytochrome *c* oxidase subunits (4, 5a, 7a, and 15), supporting mt regulation of metabolism and apoptosis (Roman et al., 2005). We also noted associations between CuZn-superoxide dismutase (SOD1) and a PD-causing protein (PARK7), suggesting a protective role against oxidative stress (Kahle et al., 2009) and mt acetyl-CoA acetyltransferase (ACAT1) binding with its downstream effector PDHA1 that was implicated in the Warburg effect and tumorigenesis (Fan et al., 2014).

Among the many previously unreported interactions in the FLAG MP network (Table S1), the interaction of dynamin-related protein (DNM1L), which mediates outer mt membrane fission, with CDK1 and its sumoylation target, SUMO2, was consistent with CDK1-dependent DNM1L phosphorylation (Taguchi et al., 2007) and adaptive mt response of DNM1L to oxidative stress (Figueroa-Romero et al., 2009). While PDHA1 is involved in alternating from oxidative phosphorylation to aerobic glycolysis in cancer cells (Hitosugi et al., 2011), we found PDHA1 to co-purify with oncoproteins (FASN, TP53) and apoptotic factors (AIFM1, ACIN1) in addition to programmed cell death 6 interacting protein (PDCD6IP), as expected (Huttlin et al., 2017), suggesting that PDHA1 is likely to play a role with proteins related to tumorigenesis. Similarly, PARK7 stably interacted with MP targets not previously reported (PDHA1, DNM1L), consistent with the role of PARK7 in the regulation of energy metabolism (Hao et al., 2010) and mt dynamics (Irrcher et al., 2010).

As a substantial number of interactions (853) overlapped between the SH-SY5Y cells and the FLAG MP network (Figure 2F), we examined these interactions for relevance to disease phenotypes in humans using genome-wide association (GWAS) disease datasets, the Human Gene Mutation Database (HGMD), and the Online Mendelian Inheritance in Man (OMIM) database. While few interacting proteins had similar disease annotations (Figure S3D), we found one-quarter (88, 26%) of the interaction partners (333) in SH-SY5Y cells had disease-associated SNPs (Figures S3E and S3F). This includes SNPs associated with nervous, metabolic, and neurodevelopmental disorders, as well as cancer and cardiovascular disease (Table S4). Notably, we confirmed three-fourths (599, 70%) of the native PPIs from SH-SY5Y cells (853) in mouse brain and/or neurons of retinoic acid-differentiated human pluripotent embryonal carcinoma NTera2 cells (a neuronal model to study NDs) by IP/MS (Figure S3G; Table S1), supporting the assembly of these macromolecules in neural processes.

Since protein complexes can be revealed from network topology as clusters of interconnected proteins (Huttlin et al., 2017), we employed the coreMethod (Leung et al., 2009) and clusterONE (Nepusz et al., 2012) algorithms to partition the 853 neuronal-relevant PPIs into multiprotein complexes, allowing examination of interactions of disease-linked protein subunits within complexes. The coreMethod algorithm yielded more functionally cohesive protein subunits having greater agreement with annotated CORUM complexes (Figure S3H), and thus was used for all subsequent analysis. Using the coreMethod, we identified 130 putative multiprotein complexes containing at least one MP (Figure 3A; Table S4), with many complexes containing fewer than four proteins (Figure 3B). Few (13, 10%) of the predicted complexes matched a curated CORUM assembly at 25% overlap or greater. Nearly half (59, 45%) were entirely unreported (Figure 3C).

Given their potential relevance to NDs, we explored 23 of the 130 predicted multiprotein assemblies where subunits within the complex were enriched ($p \leq 0.05$) for disease annotations (Figure 3D; Table S4). For example, mutations in mt-localized respiratory chain enzymes (*COQ2*, *COX15*, *PDHA1*, *SDHA*) and the phosphate carrier *SLC25A3*, which are grouped together in a single complex, are associated with mt or metabolic disorders (reviewed in OMIM), presumably through regulation of oxidative phosphorylation. Alternately, mutations in superoxide dismutase (*SOD1*), cytoskeleton-regulatory profilin (*PFN1*), and mt fission protein (*DNM1L*), which are grouped into the same complex, have been shown to cause various NDs, including ALS and epileptic encephalopathy (reviewed in OMIM). Similarly, mutations in pre-mRNA processing (*PRPF4*) and early-onset parkinsonism (*PARK7*) proteins, which form a heterodimeric complex (Table S4), was consistent with the association of retinal degeneration with systemic NDs (London et al., 2013). Overall, these observations strengthen the view that our unbiased network captures known PPIs and reveals protein pairs with physical links that can be used to generate testable hypotheses for functional discovery.

Interacting Partners in the FLAG MP Network Linked to *De Novo* Autism

Increasingly genetic, clinical, and biochemical evidence has linked mt dysfunction with ASD, yet the biological relevance of this relationship remains unclear (Rossignol and Frye, 2012). Specifically, it is unknown: (1) whether there any mtPPIs relevant to ASD that form a convergent network, (2) what common set of MPs function as key intermediates in ASD-related processes, and (3) whether interacting partners of bait MPs that are targets of key epigenetic regulators mediate ASD pathogenesis. We addressed these questions by examining the interacting partners of the FLAG MP network, and found significant ($p = 2.6 \times 10^{-8}$; $p = 5.7 \times 10^{-5}$) enrichment for mtPPIs linked to several human disorders including ASD (Figure 4A). To determine the relevance of specific interactions to ASD, we examined these interacting proteins in ASD exome-sequencing studies aimed at identifying recurrent *de novo* mutations (Table S5). We found that 46 (of 772) proteins that both interacted with mt baits and were previously

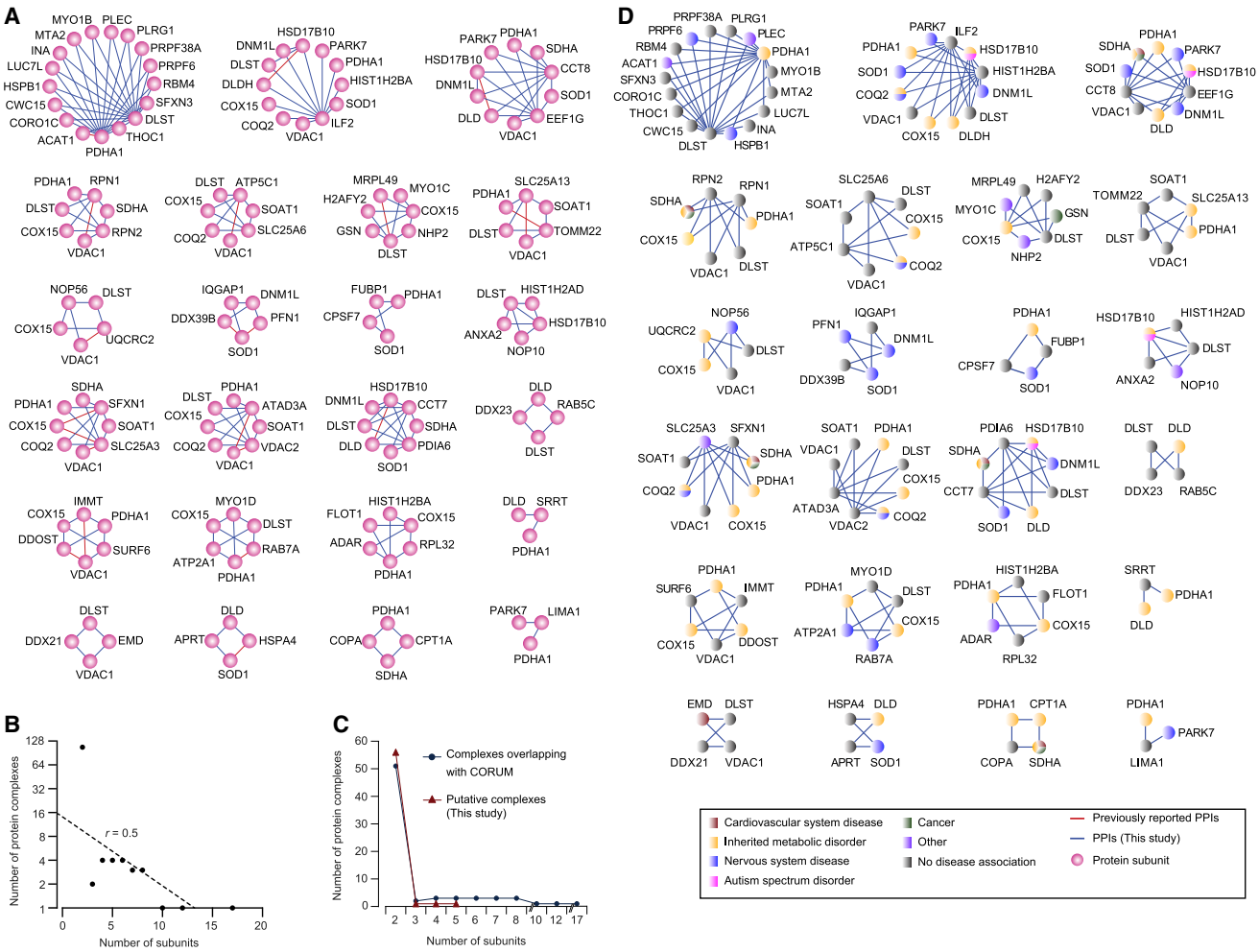

Figure 3. MP Complexes and Their Association to Human Diseases

(A) Multiprotein complexes with at least one MP are shown with PPIs (see Table S4).

(B) Subunit distribution of MP complexes.

(C) Putative MP complexes overlapping with CORUM reference complex set.

(D) MP assemblies enriched ($p \leq 0.05$) for links to the same or different types of human diseases (see Figure S3).

implicated in ASD showed positively correlated co-expression profiles (Figure 4B) in human neocortex brain development (Parikshak et al., 2013), suggesting shared functionality. Consistent with this, mammalian phenotypic enrichment analysis (reviewed in Li et al., 2015) revealed that the murine mutants for 46 ASD-linked interacting proteins were significantly enriched ($p < 10^{-3}$) for autism-associated defects, including abnormalities in mt morphology and neuronal physiology (Table S5). Also, these MP binding partners are encoded by genes that have known, rare inherited, or *de novo* mutation events in proband and/or sibling pairs (Figures 4C and S4A; Table S5) from simplex autism families (Krumm et al., 2015), suggesting these interacting proteins may be risk factors for ASD.

Finding ASD-linked interacting proteins to be co-expressed in human neocortex (Figure 4B) prompted us to survey the expression dynamics of each bait MP and their binding partners throughout cortical development (Parikshak et al., 2013). Specifically, we surveyed the co-expression of bait MPs and their binding partners from post-conception week (PCW) 8–12 months, the time period at which autistic symptoms typically develop. ASD-linked proteins, connected through 143 interactions with MP baits, co-fluctuated in expression in the early fetal (prior to PCW 17), prenatal (PCW 17–26), and postnatal (4, 10, and 12 months) brain developmental stages. These proteins also showed a decreased expression in the early fetal stage, compared with the postnatal stage (Figures 4D and S4B; Table S5), suggesting an early role of these proteins in disease origin.

Nearly half of the ASD-implicated proteins were identified as preys of mt α-ketoglutarate dehydrogenase complex subunits (PDHA1, DLST, and DLD), suggesting involvement of these proteins in the regulation of respiratory chain biogenesis (Figure 4D). One-quarter (23%, 11) of those proteins also showed convergence on a genomic region affected by copy number variants in autism (e.g., membrane-localized annexin *ANXA1* and the cytoplasmic isoleucine-tRNA synthetase *IARS* are located in 9q21; Figure S4C; Table S5). These observations and the fact

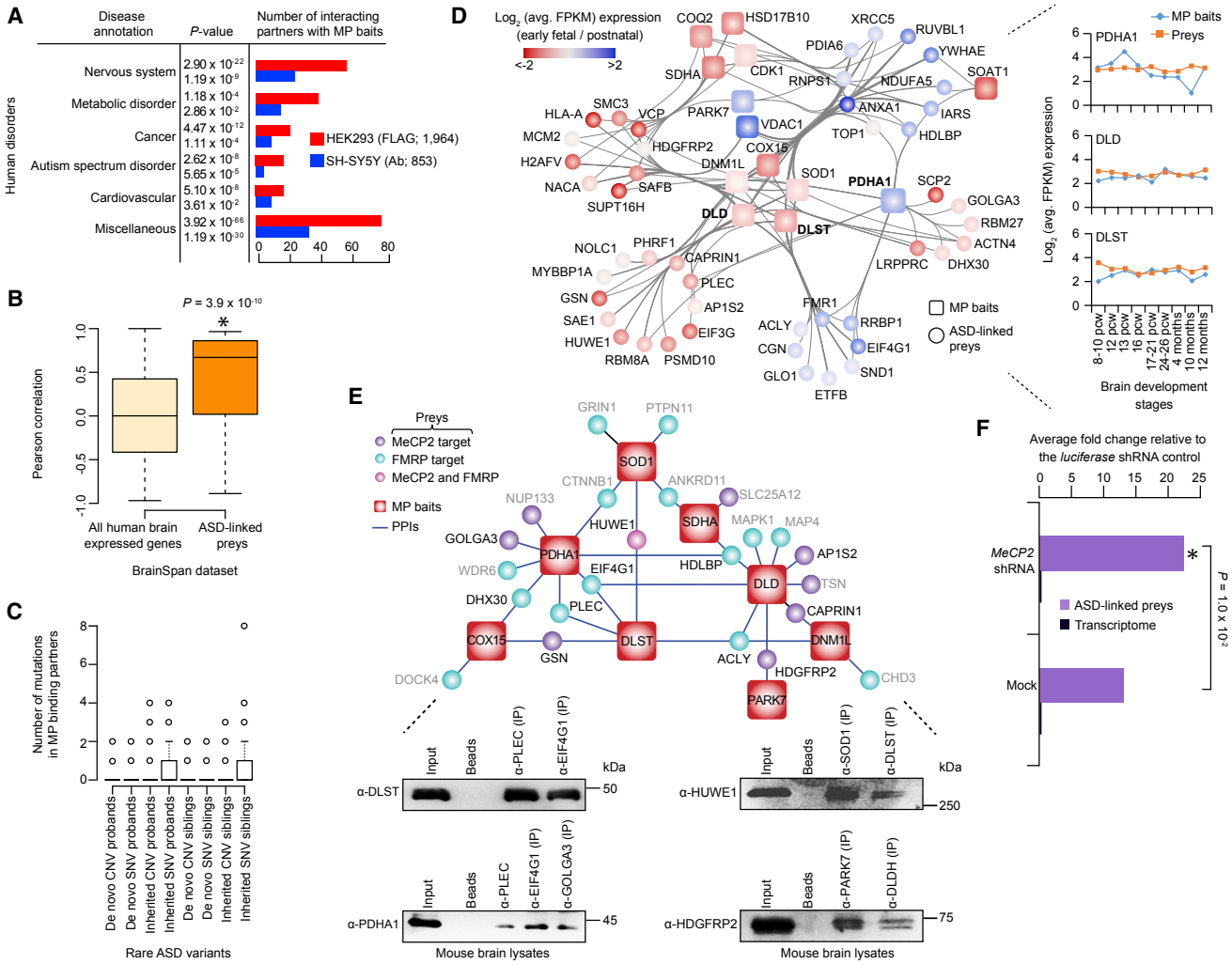

Figure 4. MP Interactions Linked to ASD

(A) Enrichment of PPIs in HEK293 or SH-SY5Y cells linked to human diseases; p values from Fisher's exact test adjusted for multiple testing by Benjamini-Hochberg method.

(B) Correlation of expression profiles for ASD-linked interacting proteins in human neocortex; *p value, Mann-Whitney-Wilcoxon test.

(C) Mutations in MP binding partners with rare ASD variants; single-nucleotide or copy number variants (SNVs, CNVs).

(D) Temporal expression pattern of bait MPs and their ASD-linked binding partners (see Figure S4; Table S5) in early fetal (red) or postnatal (blue) stages of cortical development from post-conception week (PCW) 8–12 months.

(E) Subnetwork linking MP baits with ASD-associated proteins regulated by MeCP2 and/or FMRP. Gray text indicates ASD-associated interacting proteins below the cutoff. IPs of indicated prey proteins in mouse brain lysates using protein-specific Abs. Protein G beads served as a negative control.

(F) Transcript levels of ASD-linked preys in mouse primary cortical neurons transduced with *MeCP2* shRNA (or mock) relative to *luciferase* shRNA control (Lanz et al., 2013); *p value, Student's t test.

that on average nine ASD-linked proteins interact with the same target MP ($p = 2.7 \times 10^{-11}$) suggest that the ASD-linked binding partners form a convergent network, either through a common set of MPs that mediate cellular functions linked with ASD or they function as key intermediates in ASD-related bioprocesses.

Almost a dozen of the 46 ASD-linked proteins co-purifying with MP baits were found to be regulated by syndromic autism risk factors MeCP2 (methyl CpG binding protein 2) and FMRP (fragile X mental retardation protein; Figure 4E). This finding was confirmed by immunoblotting using a protein-specific Ab (Figure 4E). Examining a transcriptomic dataset collected following shRNA *MeCP2* knockdown in mouse cortical neurons (Lanz et al., 2013), we found that the transcript levels of mouse orthologs of the 46 ASD-linked interacting proteins exhibited significant ($p = 1.0 \times 10^{-2}$; Figure 4F) upregulation upon *MeCP2* knockdown compared with mock controls. These results suggest the role of FMRP or MeCP2 in controlling ASD-relevant, mt-mediated PPIs.

ALS-Linked Mutations on SOD1-PRDX5 Binding Impair Mt Homeostasis

The FLAG MP network revealed the physical connections of superoxide dismutase (SOD1) with members of the peroxiredoxin (PRDX 2, 4, 5, and 6) antioxidant system (Table S1), as was

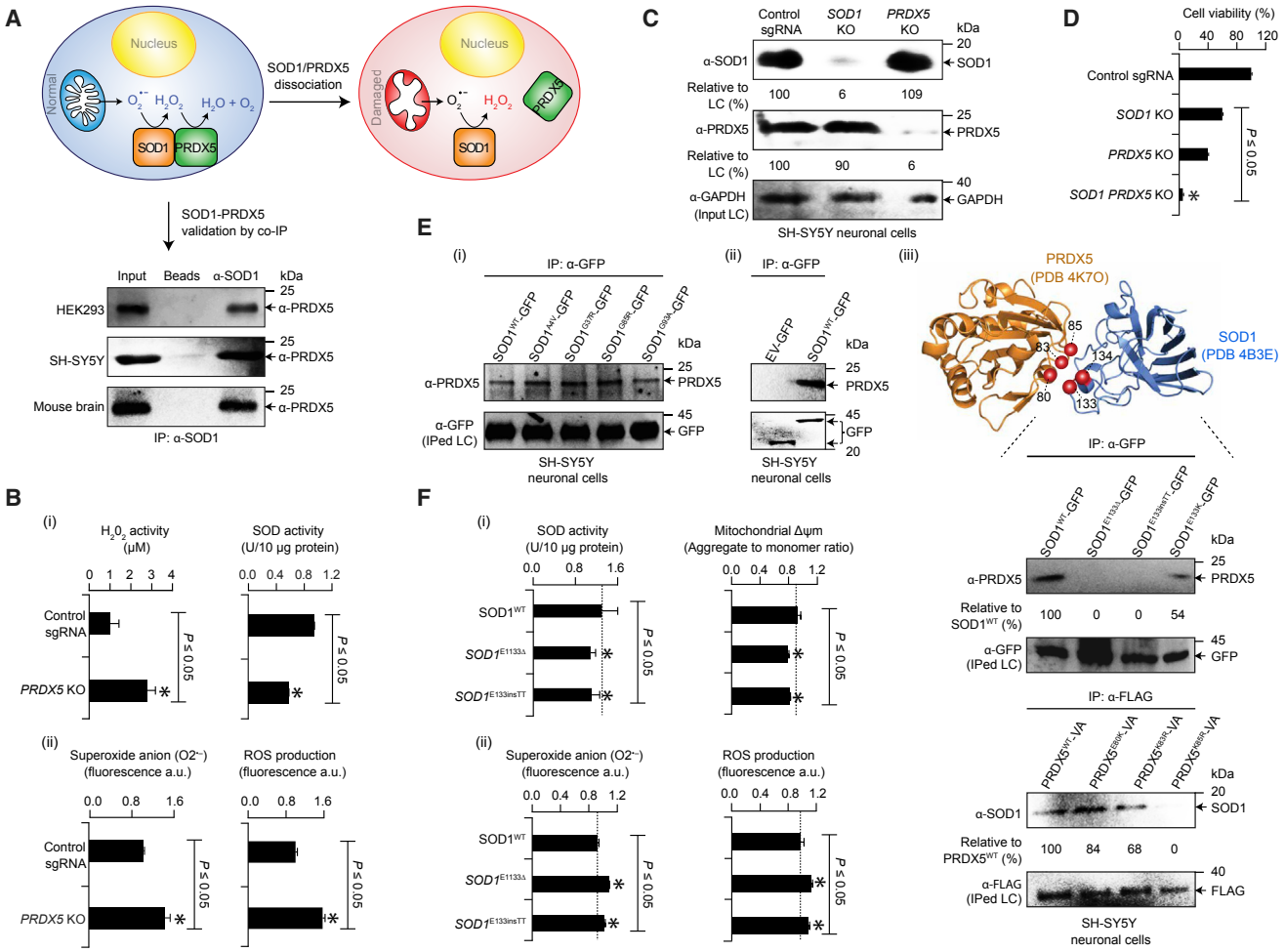

Figure 5. SOD1-PRDX5 Association in Mt Redox Homeostasis

(A) Model illustrating the role of SOD1 with PRDX5 in redox homeostasis. IPs of native SOD1 in indicated cell lysates probed with PRDX5 Ab; Protein G beads used as a negative control.

(B) H_2O_2 and SOD activity (i), as well as $O_2^{\bullet-}$ and ROS (ii) levels in control single guide RNA (sgRNA) and *PRDX5* KO SH-SY5Y cells (see also Figure S5); a.u., arbitrary units.

(C) SOD1 or PRDX5 levels in control sgRNA and KO SH-SY5Y cells with indicated Abs was normalized to input GAPDH loading control (LC).

(D) Survival of SH-SY5Y cells with KOs versus control sgRNA.

(E) IPs of WT and mutants fused with GFP or VA tag in SH-SY5Y cells (i–iii) probed with PRDX5 or SOD1 Ab. Band intensities normalized to immunoprecipitated GFP or FLAG LCs; EV, empty vector. SOD1 and PRDX5 structures (iii) with interface residues (red) mediate the interaction.

(F) SOD activity and mt membrane potential (i), as well as $O_2^{\bullet-}$ and ROS levels (ii) in SH-SY5Y cells of WT or mutant *SOD1*. Data (B, D, and F) are means ± SD (n = 3; *p ≤ 0.05, Student's t test).

recently reported (Havugimana et al., 2012; Wan et al., 2015). Here, we investigated the functional significance of a heterodimeric interaction between SOD1 and PRDX5, as the precise contribution of this association to mt function and neurodegeneration are still unclear. SOD1 is a homodimeric protein located in the cytosol and mt intermembrane space (Fischer et al., 2011) with a CuZn-SOD active site domain, while the hydrogen peroxide (H_2O_2) scavenger PRDX5, unlike other peroxiredoxins, contains a thioredoxin-like domain and is predominantly localized to the mt (Figure S5A). Both SOD1 and the peroxiredoxins, including PRDX5, are evolutionarily conserved (Figure S5A) and ubiquitously expressed in various cell types of the brain (Figure S5B).

Although the primary sequences and domain architectures are quite distinct (Figure S5A), the SOD1 binding with PRDX5 in HEK293 cells was confirmed by co-immunoprecipitation (co-IP) in SH-SY5Y cells and mouse brain lysates (Figure 5A). Subcellular fractionation analysis showed this association to occur in mt rather than in the cytosol or lysosome (Figure S5C). SOD1-catalyzed dismutation of the superoxide radical ($O_2^{\bullet-}$) to H_2O_2, which is detoxified into water and oxygen by PRDX5 (Figure 5A), is crucial for the maintenance of an appropriate mt redox environment and avoidance of cell death (Barber et al., 2006). We therefore postulated that dissociation of the SOD1-PRDX5 interaction might hamper this dismutation reaction (Figure 5A), resulting

in an increase in ROS, and consequently, mt damage and cell death.

Accordingly, CRISPR-Cas9-mediated *PRDX5* knockout (KO) in SH-SY5Y cells caused significantly increased levels of H_2O_2 and decreased total SOD activity, whereas both $O_2^{\bullet -}$ and ROS activities were elevated (Figure 5B). These effects were specific, as no alteration in SOD1 levels was observed in *PRDX5* KO (Figure 5C). The *PRDX5* KO also showed slow growth in a *SOD1* KO (Figure 5D), again indicating a functional dependency between PRDX5 and SOD1.

Since virtually 150 different *SOD1* gene mutations have implications in familial ALS (Saccon et al., 2013), screening to find if any of these mutations could perturb the SOD1-PRDX5 interaction is a laborious task. We thus implemented a two-pronged approach: first, we made use of the commercially accessible mutant *SOD1*-GFP variants (with ALS-associated *SOD1* mutations: A4V, G37R, G85R, and G93A), and finding that none of these *SOD1* mutations reliably perturbed the interaction, immunoprecipitating with PRDX5 as efficiently as WT SOD1 (Figure 5E). We next employed a molecular docking approach using crystal structures available in the PDB to determine the location of the residues supporting the SOD1-PRDX5 association. We found two residues in SOD1 at the interaction interface (E133 and E134), mutations in both of which have been linked to ALS (Saccon et al., 2013). To examine the effect of these ALS-associated mutations on the SOD1-PRDX5 interaction, we generated three mutant *SOD1*-GFP variants (E133Δ, E133insTT, and E133K). Both the E133Δ and E133insTT variants, but not E133K, completely disrupted the SOD1-PRDX5 interaction in SH-SY5Y cells (Figure 5E). Perturbation of this interaction by these ALS-linked mutations appears specific, as mutant *SOD1*-GFP variants (E133Δ and E133insTT) resulted in lower total SOD activity and mt membrane potential and higher $O_2^{\bullet -}$ and ROS activities (Figure 5F), similar to that seen in *PRDX5* KO (Figures 5B and S5D).

We further assessed if loss of interaction with a WT form of SOD1 (rather than the absence of *PRDX5*) can lead to the same phenotypic outcome by testing three (E80K, K83R, K85R) residues in *PRDX5* at the interaction interface. While these residues of *PRDX5* have never been implicated in ALS (or any other human diseases), a more comprehensive catalog of human protein-coding genetic variation study from thousands of individuals with diverse ethnicities (Lek et al., 2016) predicted the residues to have moderate (E80K), normal (K83R), and deleterious (K85R) phenotypes. IP of these three mutant *PRDX5* VA-tag variants in SH-SY5Y cells when probed with SOD1 Ab showed K85R, but not E80K or K83R variants, to disrupt the SOD1-PRDX5 association (Figure 5E) and exhibit a phenotypic outcome (Figure S5E) similar to *SOD1* variants (Figure 5F). While further *in vivo* experiments are required to understand the role of SOD1-PRDX5 binding in ALS, our data suggest an essential role in cellular redox balance and mt homeostasis.

DLD Degrades IκBε via Its Proteolytic Activity

Another notable interaction from the FLAG MP network was between dihydrolipoamide dehydrogenase (DLD), localized in the cytosol and mt of N9 microglial cells (Figure S6A), and inhibitor of NF-κB epsilon (IκBε) regulating the inflammatory processes (Figure 6A) in the nervous system (reviewed in Pradere et al., 2016). This interaction, which was verified by co-IP in N9 cells and mouse brain lysates (Figure 6B), was found to occur predominantly in the cytosol, and to a lesser extent within the mt (Figure S6B).

Typically in resting cells, NF-κB is sequestered within the cytosol by the inhibitory IκB proteins (IκBα, -β, -ε, -γ) which mask the nuclear localization signal of NF-κB. Upon activation by oxidative stress and pro-inflammatory cytokines (Figure 6A), IκB-kinase phosphorylates inhibitory IκB proteins (including IκBε) for subsequent ubiquitination and proteosomal degradation (reviewed in Pradere et al., 2016). The degraded IκB inhibitory proteins then unmask the nuclear localization signal on NF-κB, allowing free NF-κB to move into the nucleus where it binds target DNA elements and activates transcription of genes involved in the immune response, inflammation, and cell proliferation. In the case of microglial cells, activated NF-κB can lead to microglial priming to release inflammatory mediators, contributing to the progression of NDs (Perry and Holmes, 2014).

DLD can exhibit proteolytic activity under pathological conditions, including the acidification of the mt matrix due to loss of membrane potential (Babady et al., 2007). Therefore, we hypothesized that DLD might degrade IκBε, enabling NF-κB to traffic into the nucleus for activation of gene transcription. To test this, we immunoprecipitated DLD from N9 cells following rotenone or CCCP (carbonyl cyanide m-chlorophenyl hydrazine)-induced mt depolarization, finding a decrease in the levels of IκBε (Figure 6C). This change in IκBε was likely due to DLD, since the abundance of IκBε was unaffected following rotenone-mediated depolarization of mt in *DLD* KO and cells expressing an FLAG fusion of a proteolytically inactive S456A *DLD* variant (Figures 6D and S6C), suggesting that the *DLD* catalytic mutant (DLD-S456A) could act as a dominant-negative with respect to proteolytic activity. This was tested by transfecting N9 cells containing the native WT DLD with varying amounts of mutant DLD-S456A, comparing proteolytic activity against N9 cells overexpressing equivalent amounts of FLAG-tagged WT DLD alone. The IκBε tend to degrade with decreasing amounts of S456A *DLD* variant (Figure S6D), indicating DLD-S456A functions as a dominant-negative in IκBε degradation.

To ascertain if DLD degrades IκBε due to its proteolytic activity and not indirectly through the functional proteasome, the *DLD* KO N9 cells were treated with a proteasome inhibitor MG-132, alone or in combination with rotenone. The harvested cells were then immunoprecipitated with IκBε and probed with anti-ubiquitin. In contrast to N9 cells treated with MG-132, *DLD* KO showed an increase in polyubiquitination levels when treated with MG-132 alone or in combination with rotenone (Figure 6E). This suggests that IκBε degradation by DLD via its proteolytic activity is independent of proteasomal function.

Given our observed interactions between DLD/IκBε and PD-causative proteins, PARK7, PINK1 (PTEN-induced putative kinase 1), and PARKIN (E3 ubiquitin ligase), as confirmed in mouse brain lysates (Figure S6E), we examined if DLD-mediated IκBε degradation occurs by PINK1/PARKIN. The mt fraction isolated from *DLD* KO cells showed PINK1 translocation to the mt as in control N9 rotenone-treated cells (Figure 6F), indicating that under depolarizing conditions, DLD may not degrade IκBε by PINK1/PARKIN.

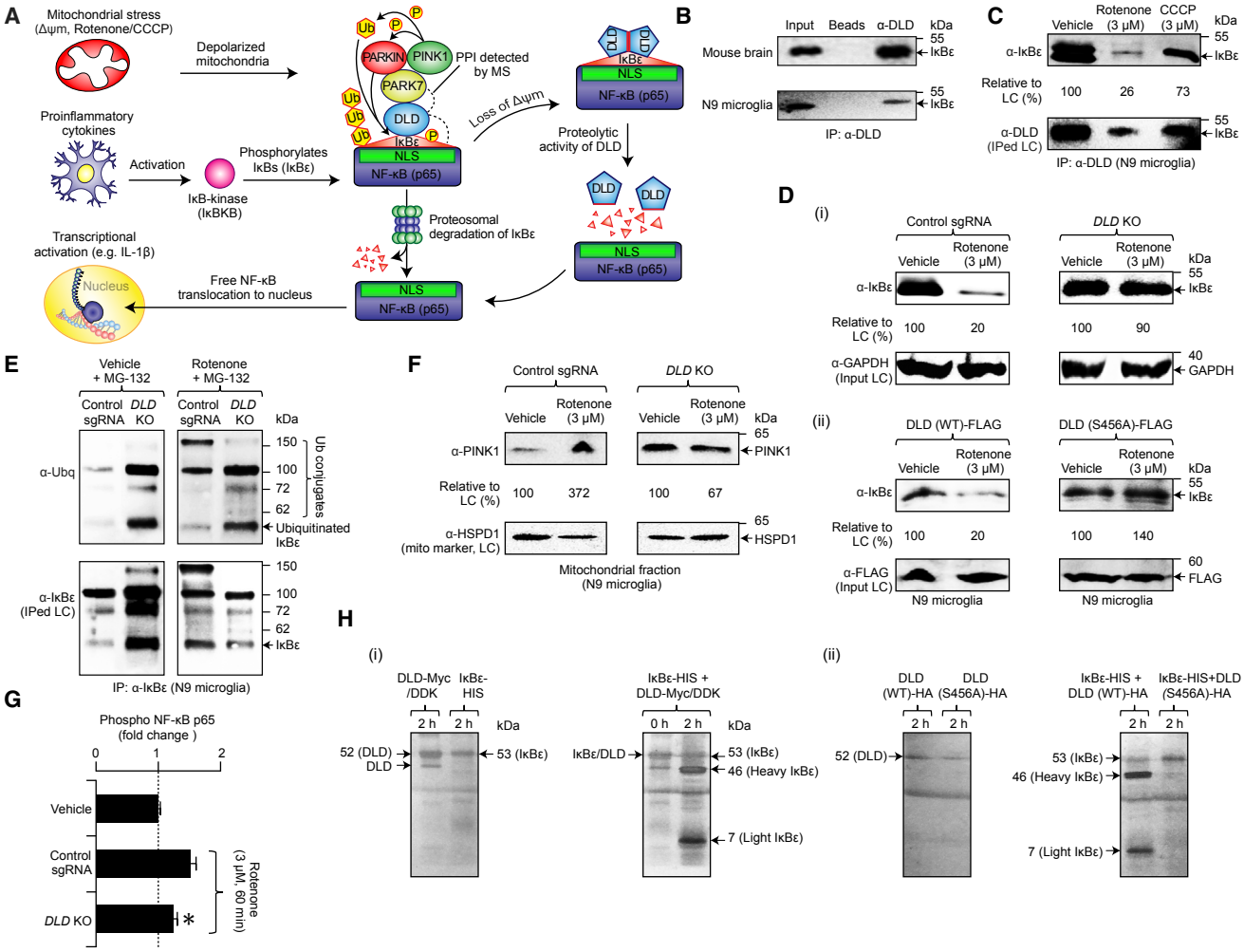

Figure 6. Proteolytic Activity of DLD in IκBε Degradation

(A) Proposed model for IκBε degradation by DLD.

(B and C) IPs of DLD in the absence (B) or presence (C) of stressors or vehicle (0.003% v/v dimethylformamide [DMF]) in mouse brain or N9 lysates probed with IκBε Ab. Protein G beads used as a negative control. Band intensities normalized to immunoprecipitated DLD loading control (LC).

(D) IκBε levels in *DLD* KO (i) and proteolytically inactive (S456A) mutant (ii) with respective WT controls in N9 cells treated with stressor or vehicle probed with IκBε Ab. Band intensities normalized to input GAPDH or FLAG LC.

(E) IPs of IκBε in control sgRNA or *DLD* KO N9 cells treated with MG-132 in the presence of stressor or vehicle probed with ubiquitin (Ubq) Ab.

(F) Mt fraction isolated from control sgRNA or *DLD* KO N9 cells treated with stressor or vehicle probed with PINK1 Ab. Band intensities normalized to HSPD1 mt marker LC.

(G) p65 phosphorylation level in control sgRNA or *DLD* KO N9 cells with rotenone treated for 60 min over vehicle. Data are means ± SD (n = 6; *p ≤ 0.05, Student's t test).

(H) Silver stain gel portraying IκBε cleavage products in the (i) indicated recombinant proteins and/or (ii) HA-fused DLD WT or catalytic (S456A) mutant at 0 or 2 hr post IκBε-HIS addition. The cleavage products corresponding to DLD or IκBε in silver stain gel were determined by MS (see also Figure S6).

Next, given its ability to degrade IκBε (Figure 6C), we sought to evaluate if DLD has any underlying role in the activation of NF-κB. To determine this, we examined the p65 subunit of NF-κB, which is involved in neuronal inflammation (Pradere et al., 2016). Since serine phosphorylation of nuclear p65 at residue 536 of NF-κB is commonly used to quantify NF-κB activation (reviewed in Pradere et al., 2016), we measured the phosphorylation of p65 in the nuclear extracts of rotenone-treated control and *DLD* KO N9 cells. After treatment with CCCP, we observed a ~1.4 ± 0.4-fold increase in p65 phosphorylation in N9 cells, confirming that, like rotenone (Gao et al., 2013), CCCP can directly induce NF-κB activation (Figure S6F). However, we found significantly ($p \leq 0.05$) less p65 phosphorylation in *DLD* KO cells treated with rotenone compared with control N9 cells (Figure 6G). Activated microglia can augment neuroinflammation by secreting various neurotoxic and pro-inflammatory cytokines such as interleukin (IL)-1β. These cytokines also play a key role in NF-κB activation, neuronal damage, and degeneration (reviewed in Kaltschmidt and Kaltschmidt, 2009). We therefore measured the mRNA expression of this inflammatory mediator by real-time qPCR in control and *DLD* KO N9 cells following rotenone treatment.

As with p65 phosphorylation (Figure 6G), we found an average ~5.2 ± 0.9-fold increase in the mRNA expression of the NF-κB-driven IL-1β inflammatory mediator in N9 cells treated with rotenone, whereas the expression of this mediator was substantially ($p \leq 0.05$) reduced in rotenone-treated *DLD* KO cells (Figure S6G). These results suggest that NF-κB activation and IκBε degradation are dependent on DLD in microglia.

In line with these findings, the *in vitro* proteolytic activity of IκBε analyzed by silver staining showed a predominant protein band of ≈53 kDa in the reaction containing the Myc/DDK-tagged human recombinant DLD or HA-tagged proteolytic deficient *DLD* mutant (DLD-S456A) incubated with the HIS-tagged human IκBε recombinant protein for 0 or 2 hr, respectively. The proteolytic activity of the prime band (≈53 kDa) was slightly reduced, and two additional bands instead appeared with a molecular mass of ≈46 and ≈7 kDa (Figure 6H) in reactions containing the Myc/DDK- or HA-tagged WT DLD, but not in the HA-tagged mutant DLD-S456A, after 2 hr incubation with HIS-tagged IκBε. These bands represented the cleavage products of the 53 kDa fragment that matched the sequence of human IκBε (78% coverage) by MS analysis. Peptide sequence mapping of the two IκBε cleavage products from MS further showed the site of cleavage between Arg-433 and Met-444 (Figure S6H). These results suggest a previously unrecognized mechanism of IκBε degradation by the proteolytic activity of DLD.

PINK1/PARKIN Coupling to IκBε in NF-kB Is Relevant for PD *In Vivo*

Biochemical and genetic studies (reviewed in Pickrell and Youle, 2015) have revealed that PINK1 accumulation following mt depolarization stimulates the PARKIN E3 ligase through phosphorylation within its ubiquitin-like domain (Figure 7A). PARKIN then linearly ubiquitinates outer mt membrane proteins to trigger mt aggregation and selective autophagic removal of the damaged mt via mitophagy (Pickrell and Youle, 2015). The IκBε interaction with PINK1 or PARKIN was observed in cytosol, mt, and lysosome fractions (Figure S6B), possibly reflecting the shuttling of these proteins between compartments under physiologic conditions. We also observed strong binding of IκBε with PINK1/PARKIN in mouse brain lysates (Figure S6E) and reduced interaction in the fibroblasts of PD patients with *PINK1* or *PARKIN* harboring various pathogenic mutations compared with fibroblasts from healthy controls (Figure 7B). The latter observation is bona fide as these mutants were expressed (Okatsu et al., 2012; Zanellati et al., 2015) and consistent with their expected protein length (Table S6). These results led us to hypothesize that upon mt depolarization, IκBε is phosphorylated and ubiquitinated by PINK1 and PARKIN, respectively, and then degraded by the proteasome, leading to the activation of NF-κB. Consistent with our assertion, depolarization of mt by rotenone/CCCP in N9 cells increased serine phosphorylation and ubiquitination (Figure 7C) of IκBε. A similar increase in ubiquitination accumulation was also detected in rotenone-treated N9 cells following addition of an MG-132 proteasome inhibitor (Figure 7C), indicating that polyubiquitination of IκBε under depolarizing conditions tend to increase even after blocking the proteasome. *PINK1* and *PARKIN* KOs in N9 cells as well as their mutations in PD patient fibroblasts suppressed these effects (Figures 7B–7D and S6I). This suggests that phosphorylation and ubiquitination of IκBε are stimulated in PINK1- and PARKIN-dependent manners, respectively.

To further examine if IκBε can activate NF-κB following phosphorylation and ubiquitination by PINK1/PARKIN, phosphorylation of p65 was measured in the nuclear extracts of *PINK1* and *PARKIN* KOs of N9 cells treated with rotenone. We found a significant ($p \leq 0.05$) p65 phosphorylation reduction in *PINK1* and *PARKIN* KOs of N9 cells at 60 min post rotenone addition (Figure 7E). This suggests that rotenone-induced depolarization in microglia induces PINK1 and PARKIN to activate NF-κB. Similarly, the expression of an archetypal pro-inflammatory cytokine that activates NF-κB, IL-1β, was strongly ($p \leq 0.05$) suppressed in *PINK1* and *PARKIN* KOs after rotenone treatment but not in control N9 cells (Figure S6G). PINK1 activation of NF-κB in response to mt depolarization was further tested using CCCP-induced depolarized N9 cells treated with kinetin, a neo-substrate kinetin triphosphate precursor that restores mutated *PINK1* function and enhances PINK1 activity (Hertz et al., 2013). A significant increase in p65 phosphorylation was observed in N9 cells treated with kinetin alone or when combined with CCCP (Figure 7F), confirming that PINK1 activates NF-κB in N9 cells. While these results suggest IκBε phosphorylation by PINK1 or ubiquitination by PARKIN is crucial in PD patient fibroblasts, we show the mechanistic basis of these interacting PD-related molecular players in the activation of NF-κB via IκBε.

DISCUSSION

Despite being one of the most heavily studied cellular organelles, human MPs are still underrepresented in proteomic studies of physical interactions, impeding a systems-level understanding of mt biology and the development of effective therapeutics to treat diverse disorders of mt origin. The systematic proteomic analysis presented in this study offers a practical strategy to survey PPIs for all nuclear-encoded MPs in human cells. Due to the complexity of NDs, no cellular model can truly recapitulate ND states. However, we used a multi-cell-line approach to generate mt PPI network, to provide us with as many ND-relevant interactions as possible. Rigorous verification of these interactions using several complementary experimental approaches, including an AP/MS screen consisting of multiple biological replicates using the same bait MP, and verification in distinct neuronal cell lineages and mouse brain, allowed us to confidently expand the composition of known complexes, providing opportunities for functional inference.

Among the PPIs observed, our network revealed previously overlooked associations in mt redox homeostasis and NF-κB. These links were substantiated by additional biochemical and genetic experiments, providing molecular mechanistic evidence of, among others, a SOD1-PRDX5 interaction critical for mt ROS production and detoxification. Our investigation of the IκBε-PINK1/PARKIN association in N9 cells has also yielded substantial findings, notably: (1) during mt depolarization, IκBε phosphorylation and ubiquitination are reliant on PINK1 and PARKIN, respectively; (2) the edgetic mutations in *PINK1*/*PARKIN* PD patient fibroblasts perturb the IκBε binding, phosphorylation, and ubiquitination, linking genotype to phenotype relationships; (3) PINK1-PARKIN are capable of activating the NF-κB via IκBε in a manner that has implications for PD; and (4) contrary to known

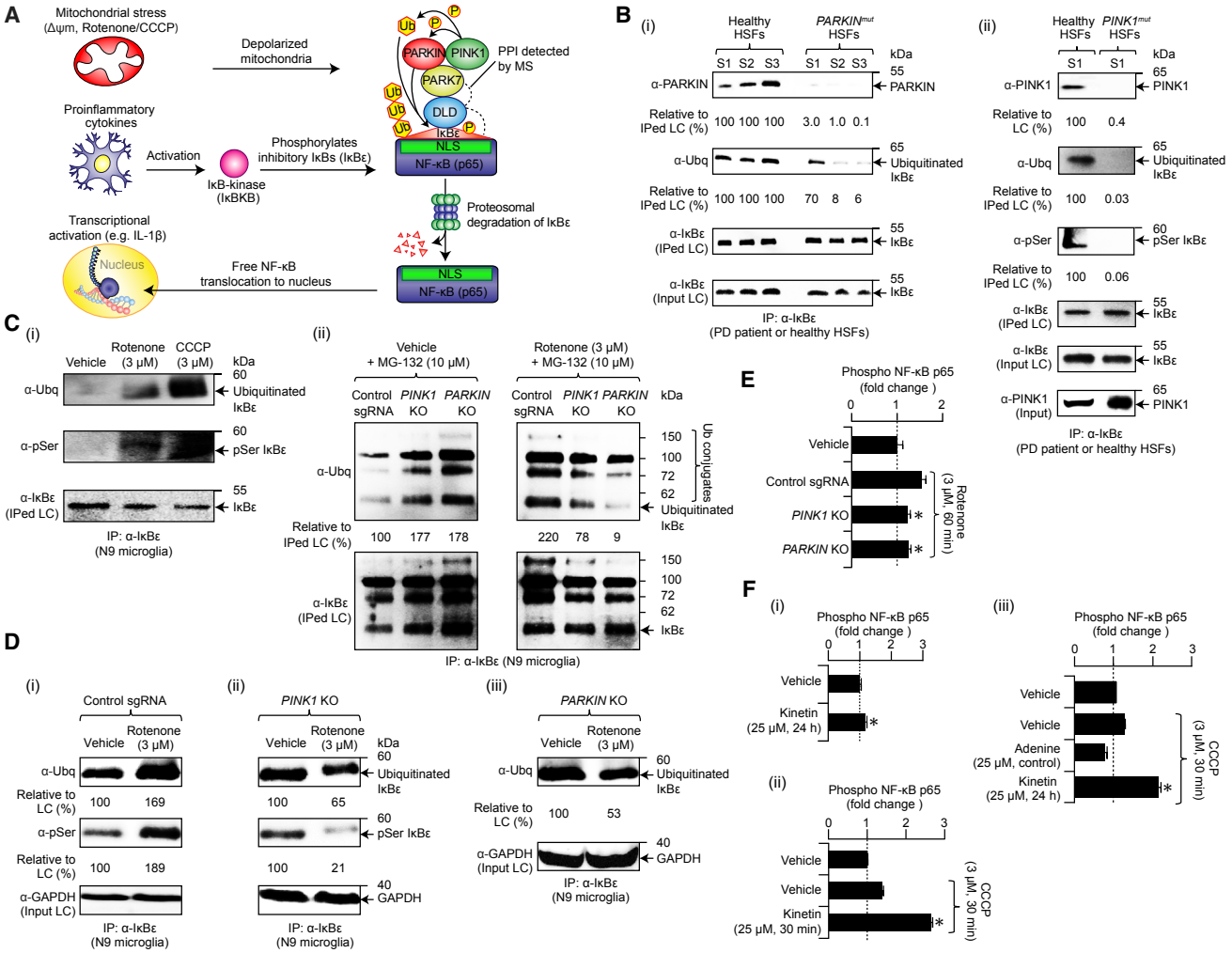

Figure 7. ND-Linked Factors Participate with IκBε in NF-κB

(A) Model for IκBε with PINK1-PARKIN in NF-κB.

(B) IPs of IκBε in healthy human skin fibroblasts (HSFs) and PD patient fibroblasts (S1–S3; Table S6) with *PARKIN* or *PINK* mutations probed with the indicated Abs; Ubq, ubiquitin; pSer, phosphoserine. Band intensities normalized against immunoprecipitated IκBε LC.

(C and D) IPs of IκBε in WT or KO N9 cells treated with (C-ii) or without (C-i; Di-iii) MG-132 and/or stressor or vehicle (0.003% DMF) probed with Ubq or pSer Ab. Band intensities normalized to immunoprecipitated IκBε or input GAPDH LC.

(E and F) p65 phosphorylation level measured in KO (E) or WT (Fi-iii) N9 cells treated with or without kinetin and/or in combination with stressor or vehicle at indicated time points. Data (E and F) are means ± SD (n = 3–6; *p ≤ 0.05, Student's t test).

kinetin application to inhibit apoptosis of human neurons in a PINK1-dependent manner (Hertz et al., 2013), CCCP-induced depolarization and kinetin-treated N9 cells that show a significant increase in NF-κB activation via PINK1 suggests that enhancing NF-κB activation in microglial cells by kinetin may contribute to neuronal inflammation and neurodegeneration. Similarly, the proteolytic effects of DLD on IκBε, detected in N9 cells, suggest a proteasomal degradation-independent mechanism of NF-κB activation upon mt stress. Overall, these insights into the biology of IκBε with PINK1-PARKIN or DLD in NF-kB deepen our understanding of neurological inflammation, with potential applications to PD pathogenesis.

Through a broader network-driven approach, we were able to show a testable disease-relevant outcome by highlighting an extensive subnetwork of ASD-linked components interacting with MPs. This includes providing insights on MPs regulated by the targets of key epigenetic regulators, MeCP2 and FMRP. While in-depth experimentation is required to solidify our understanding of mtPPIs relevant to MeCP2/FMRP-mediated ASD pathogenesis, our study clearly identifies a role of the MP network in ASD. While the network-based proteomics approach we used for ND-linked MPs illustrates the utility in capturing both stable and transient interactions to dissect mt (or disease) biology, experimental limitations exist with AP/MS-based protein interaction detection. For example, affinity tagging can potentially interfere with protein localization and interactions, even modest overexpression of some MP baits can be toxic to human cells, detergent solubilization may disrupt hydrophobic interactions, and model cell lines used may not recapitulate all relevant processes in human neurons (Babu et al., 2012; Hosp et al., 2015).

To limit these confounding effects, we avoided artifacts from overexpression by considering only PPIs from the tagged bait MPs that were captured consistently when the same set of endogenously expressed MPs were purified with protein-specific Abs in HEK293 and/or SH-SY5Y cells. Also, we found that PPIs from biological replicates that surpass NSAF scoring thresholds provided PPIs with a reduced overall false-positive rate.

Analysis of the MP network suggests that this AP/MS workflow can conceptually be applied globally for all human (or disease-linked) MPs as a means to examine the specificity and stability of MP complexes. Exploration of how disease-associated variants affect interactions among these complex members could identify avenues for therapeutic design for the vast assembly of mt diseases. By providing access to the PPI data via a public repository (PRIDE), we have presented a resource for hypothesis generation to spur further exploration of the unique biology of mt at a systems level.

STAR★METHODS

Detailed methods are provided in the online version of this paper and include the following:

- KEY RESOURCES TABLE
- CONTACT FOR REAGENT AND RESOURCE SHARING
- EXPERIMENTAL MODEL AND SUBJECT DETAILS
  - Cell Culture and Differentiation
  - Human Skin Fibroblasts Cell Culture
  - Preparation of Mouse Brain Lysates
- METHOD DETAILS
  - Target MP Selection
  - Gateway Cloning
  - Stable Cell Line Generation
  - Determining MOI
  - Crosslinking
  - Cytosolic, Mt, and Lysosomal Isolation
  - AP/MS and IP/MS Screens
  - Immunoblotting
  - Immunofluorescence
  - Validating mtPPIs by PCP BN-PAGE
  - Generation of KO Cells
  - Mutagenesis
  - Structural Modeling
  - Cellular, NF-κB, and Proteolytic Assays
  - Quantitative Real-Time PCR
- QUANTIFICATION AND STATISTICAL ANALYSIS
  - Protein Identification, NSAF Scoring, and Data Filtering
  - CoreMethod and Other Bioinformatic Analyses
  - Statistical Tests
- DATA AND SOFTWARE AVAILABILITY

SUPPLEMENTAL INFORMATION

Supplemental Information includes six figures and six tables and can be found with this article online at https://doi.org/10.1016/j.cels.2017.10.010.

AUTHOR CONTRIBUTIONS

M.B. conceived and supervised the project. R.H.M. designed the follow-up experiments and performed cell cultures, mutagenesis, tagging, imaging, and cellular assays. H.A., S.A., S.K., V.S., V.D., H.A.-T., and Z.W. contributed to MP purifications, cell-line generation, and immunoblotting. Z.M., N.E.S., and M.M. performed MS, co-fractionation, and structural modeling, respectively. A.K., S.P., Q.Z., F.G., X.X., and J.V. analyzed PPI data. R.H.M. and M.B. wrote the manuscript, with input from G.M., M.J., J.V., B.P., L.J.F., T.A., B.G., H.Y., G.D.B., K.N., and J.P. All authors read and approved the manuscript.

ACKNOWLEDGMENTS

R.H.M., M.J., and J.V. were supported by Saskatchewan Health Research Foundation Postdoctoral Fellowships, Z.W is supported by Frederick Banting and Charles Best Canada Graduate Scholarship, and M.B. is a Canadian Institutes of Health Research (CIHR) New Investigator (MSH-130178). This work was supported by grants from the CIHR to L.J.F. (MOP-77688) and M.B (MOP-125952; RSN-124512, 132191; and FDN-154318); as well as the Parkinson Society Canada (2014-673), Saskatchewan Health Research Foundation (RSN-124512), and the NIH (R01GM106019) to M.B.

Received: January 10, 2017
Revised: June 26, 2017
Accepted: October 12, 2017
Published: November 8, 2017

REFERENCES

Babady, N.E., Pang, Y.P., Elpeleg, O., and Isaya, G. (2007). Cryptic proteolytic activity of dihydrolipoamide dehydrogenase. Proc. Natl. Acad. Sci. USA *104*, 6158–6163.

Babu, M., Vlasblom, J., Pu, S., Guo, X., Graham, C., Bean, B.D.M., Burston, H.E., Vizeacoumar, F.J., Snider, J., Phanse, S., et al. (2012). Interaction landscape of membrane-protein complexes in *Saccharomyces cerevisiae*. Nature *489*, 585–589.

Barabasi, A.L., Gulbahce, N., and Loscalzo, J. (2011). Network medicine: a network-based approach to human disease. Nat. Rev. Genet. *12*, 56–68.

Barber, S.C., Mead, R.J., and Shaw, P.J. (2006). Oxidative stress in ALS: a mechanism of neurodegeneration and a therapeutic target. Biochim. Biophys. Acta *1762*, 1051–1067.

Calvo, S.E., Clauser, K.R., and Mootha, V.K. (2016). MitoCarta2.0: an updated inventory of mammalian mitochondrial proteins. Nucleic Acids Res. *44*, D1251–D1257.

Fan, J., Shan, C., Kang, H.B., Elf, S., Xie, J., Tucker, M., Gu, T.L., Aguiar, M., Lonning, S., Chen, H., et al. (2014). Tyr phosphorylation of PDP1 toggles recruitment between ACAT1 and SIRT3 to regulate the pyruvate dehydrogenase complex. Mol. Cell *53*, 534–548.

Figueroa-Romero, C., Iniguez-Lluhi, J.A., Stadler, J., Chang, C.R., Arnoult, D., Keller, P.J., Hong, Y., Blackstone, C., and Feldman, E.L. (2009). SUMOylation of the mitochondrial fission protein Drp1 occurs at multiple nonconsensus sites within the B domain and is linked to its activity cycle. FASEB J. *23*, 3917–3927.

Fischer, L.R., Igoudjil, A., Magrane, J., Li, Y., Hansen, J.M., Manfredi, G., and Glass, J.D. (2011). SOD1 targeted to the mitochondrial intermembrane space prevents motor neuropathy in the Sod1 knockout mouse. Brain *134*, 196–209.

Floyd, B.J., Wilkerson, E.M., Veling, M.T., Minogue, C.E., Xia, C., Beebe, E.T., Wrobel, R.L., Cho, H., Kremer, L.S., Alston, C.L., et al. (2016). Mitochondrial protein interaction mapping identifies regulators of respiratory chain function. Mol. Cell *63*, 621–632.

Gao, F., Chen, D., Hu, Q., and Wang, G. (2013). Rotenone directly induces BV2 cell activation via the p38 MAPK pathway. PLoS One *8*, e72046.

Hao, L.Y., Giasson, B.I., and Bonini, N.M. (2010). DJ-1 is critical for mitochondrial function and rescues PINK1 loss of function. Proc. Natl. Acad. Sci. USA *107*, 9747–9752.

Havugimana, P.C., Hart, G.T., Nepusz, T., Yang, H., Turinsky, A.L., Li, Z., Wang, P.I., Boutz, D.R., Fong, V., Phanse, S., et al. (2012). A census of human soluble protein complexes. Cell *150*, 1068–1081.

Hein, M.Y., Hubner, N.C., Poser, I., Cox, J., Nagaraj, N., Toyoda, Y., Gak, I.A., Weisswange, I., Mansfeld, J., Buchholz, F., et al. (2015). A human interactome in three quantitative dimensions organized by stoichiometries and abundances. Cell *163*, 712–723.

Hertz, N.T., Berthet, A., Sos, M.L., Thorn, K.S., Burlingame, A.L., Nakamura, K., and Shokat, K.M. (2013). A neo-substrate that amplifies catalytic activity of Parkinson's-disease-related kinase PINK1. Cell *154*, 737–747.

Hitosugi, T., Fan, J., Chung, T.W., Lythgoe, K., Wang, X., Xie, J., Ge, Q., Gu, T.L., Polakiewicz, R.D., Roesel, J.L., et al. (2011). Tyrosine phosphorylation of mitochondrial pyruvate dehydrogenase kinase 1 is important for cancer metabolism. Mol. Cell *44*, 864–877.

Hosp, F., Vossfeldt, H., Heinig, M., Vasiljevic, D., Arumughan, A., Wyler, E., Genetic and Environmental Risk for Alzheimer's Disease GERAD1 Consortium, Landthaler, M., Hubner, N., Wanker, E.E., et al. (2015). Quantitative interaction proteomics of neurodegenerative disease proteins. Cell Rep. *11*, 1134–1146.

Huttlin, E.L., Bruckner, R.J., Paulo, J.A., Cannon, J.R., Ting, L., Baltier, K., Colby, G., Gebreab, F., Gygi, M.P., Parzen, H., et al. (2017). Architecture of the human interactome defines protein communities and disease networks. Nature *545*, 505–509.

Irrcher, I., Aleyasin, H., Seifert, E.L., Hewitt, S.J., Chhabra, S., Phillips, M., Lutz, A.K., Rousseaux, M.W., Bevilacqua, L., Jahani-Asl, A., et al. (2010). Loss of the Parkinson's disease-linked gene DJ-1 perturbs mitochondrial dynamics. Hum. Mol. Genet. *19*, 3734–3746.

Kahle, P.J., Waak, J., and Gasser, T. (2009). DJ-1 and prevention of oxidative stress in Parkinson's disease and other age-related disorders. Free Radic. Biol. Med. *47*, 1354–1361.

Kaltschmidt, B., and Kaltschmidt, C. (2009). NF-kappaB in the nervous system. Cold Spring Harb. Perspect. Biol. *1*, a001271.

Kanda, A., Noda, K., and Ishida, S. (2015). ATP6AP2/(pro)renin receptor contributes to glucose metabolism via stabilizing the pyruvate dehydrogenase E1 beta subunit. J. Biol. Chem. *290*, 9690–9700.

Krumm, N., Turner, T.N., Baker, C., Vives, L., Mohajeri, K., Witherspoon, K., Raja, A., Coe, B.P., Stessman, H.A., He, Z.X., et al. (2015). Excess of rare, inherited truncating mutations in autism. Nat. Genet. *47*, 582–588.

Lanz, T.A., Guilmette, E., Gosink, M.M., Fischer, J.E., Fitzgerald, L.W., Stephenson, D.T., and Pletcher, M.T. (2013). Transcriptomic analysis of genetically defined autism candidate genes reveals common mechanisms of action. Mol. Autism *4*, 45.

Lek, M., Karczewski, K.J., Minikel, E.V., Samocha, K.E., Banks, E., Fennell, T., O'Donnell-Luria, A.H., Ware, J.S., Hill, A.J., Cummings, B.B., et al. (2016). Analysis of protein-coding genetic variation in 60,706 humans. Nature *536*, 285–291.

Leung, H.C., Xiang, Q., Yiu, S.M., and Chin, F.Y. (2009). Predicting protein complexes from PPI data: a core-attachment approach. J. Comput. Biol. *16*, 133–144.

Li, J., Ma, Z., Shi, M., Malty, R.H., Aoki, H., Minic, Z., Phanse, S., Jin, K., Wall, D.P., Zhang, Z., et al. (2015). Identification of human neuronal protein complexes reveals biochemical activities and convergent mechanisms of action in autism spectrum disorders. Cell Syst. *1*, 361–374.

London, A., Benhar, I., and Schwartz, M. (2013). The retina as a window to the brain-from eye research to CNS disorders. Nat. Rev. Neurol. *9*, 44–53.

Malty, R.H., Jessulat, M., Jin, K., Musso, G., Vlasblom, J., Phanse, S., Zhang, Z., and Babu, M. (2015). Mitochondrial targets for pharmacological intervention in human disease. J. Proteome Res. *14*, 5–21.

Nepusz, T., Yu, H., and Paccanaro, A. (2012). Detecting overlapping protein complexes in protein-protein interaction networks. Nat. Methods *9*, 471–472.

Ning, K., Fermin, D., and Nesvizhskii, A.I. (2012). Comparative analysis of different label-free mass spectrometry based protein abundance estimates and their correlation with RNA-Seq gene expression data. J. Proteome Res. *11*, 2261–2271.

Nunnari, J., and Suomalainen, A. (2012). Mitochondria: in sickness and in health. Cell *148*, 1145–1159.

Okatsu, K., Oka, T., Iguchi, M., Imamura, K., Kosako, H., Tani, N., Kimura, M., Go, E., Koyano, F., Funayama, M., et al. (2012). PINK1 autophosphorylation upon membrane potential dissipation is essential for Parkin recruitment to damaged mitochondria. Nat. Commun. *3*, 1016.

Pagliarini, D.J., Calvo, S.E., Chang, B., Sheth, S.A., Vafai, S.B., Ong, S.E., Walford, G.A., Sugiana, C., Boneh, A., Chen, W.K., et al. (2008). A mitochondrial protein compendium elucidates complex I disease biology. Cell *134*, 112–123.

Parikshak, N.N., Luo, R., Zhang, A., Won, H., Lowe, J.K., Chandran, V., Horvath, S., and Geschwind, D.H. (2013). Integrative functional genomic analyses implicate specific molecular pathways and circuits in autism. Cell *155*, 1008–1021.

Perry, V.H., and Holmes, C. (2014). Microglial priming in neurodegenerative disease. Nat. Rev. Neurol. *10*, 217–224.

Pickrell, A.M., and Youle, R.J. (2015). The roles of PINK1, parkin, and mitochondrial fidelity in Parkinson's disease. Neuron *85*, 257–273.

Pradere, J.P., Hernandez, C., Koppe, C., Friedman, R.A., Luedde, T., and Schwabe, R.F. (2016). Negative regulation of NF-kappaB p65 activity by serine 536 phosphorylation. Sci. Signal. *9*, ra85.

Roman, I., Figys, J., Steurs, G., and Zizi, M. (2005). In vitro interactions between the two mitochondrial membrane proteins VDAC and cytochrome C oxidase. Biochemistry *44*, 13192–13201.

Rosner, M., Schipany, K., and Hengstschlager, M. (2013). Merging high-quality biochemical fractionation with a refined flow cytometry approach to monitor nucleocytoplasmic protein expression throughout the unperturbed mammalian cell cycle. Nat. Protoc. *8*, 602–626.

Rossignol, D.A., and Frye, R.E. (2012). Mitochondrial dysfunction in autism spectrum disorders: a systematic review and meta-analysis. Mol. Psychiatry *17*, 290–314.

Saccon, R.A., Bunton-Stasyshyn, R.K., Fisher, E.M., and Fratta, P. (2013). Is SOD1 loss of function involved in amyotrophic lateral sclerosis? Brain *136*, 2342–2358.

Scott, N.E., Rogers, L.D., Prudova, A., Brown, N.F., Fortelny, N., Overall, C.M., and Foster, L.J. (2017). Interactome disassembly during apoptosis occurs independent of caspase cleavage. Mol. Syst. Biol. *13*, 906.

Taguchi, N., Ishihara, N., Jofuku, A., Oka, T., and Mihara, K. (2007). Mitotic phosphorylation of dynamin-related GTPase Drp1 participates in mitochondrial fission. J. Biol. Chem. *282*, 11521–11529.

van de Leemput, J., Boles, N.C., Kiehl, T.R., Corneo, B., Lederman, P., Menon, V., Lee, C., Martinez, R.A., Levi, B.P., Thompson, C.L., et al. (2014). CORTECON: a temporal transcriptome analysis of in vitro human cerebral cortex development from human embryonic stem cells. Neuron *83*, 51–68.

Wan, C., Borgeson, B., Phanse, S., Tu, F., Drew, K., Clark, G., Xiong, X., Kagan, O., Kwan, J., Bezginov, A., et al. (2015). Panorama of ancient metazoan macromolecular complexes. Nature *525*, 339–344.

Wang, M., Weiss, M., Simonovic, M., Haertinger, G., Schrimpf, S.P., Hengartner, M.O., and von Mering, C. (2012). PaxDb, a database of protein abundance averages across all three domains of life. Mol. Cell. Proteomics *11*, 492–500.

Zanellati, M.C., Monti, V., Barzaghi, C., Reale, C., Nardocci, N., Albanese, A., Valente, E.M., Ghezzi, D., and Garavaglia, B. (2015). Mitochondrial dysfunction in Parkinson disease: evidence in mutant PARK2 fibroblasts. Front. Genet. *6*, 78.

STAR★METHODS

KEY RESOURCES TABLE

REAGENT or RESOURCE	SOURCE	IDENTIFIER
Antibodies		
Anti-FLAG	Sigma-Aldrich	Cat# F1804; RRID: AB_262044
Anti-VDAC1	ProteinTech	Cat# 10866-1-AP; RRID: AB_2257153
Anti-PINK1	Abcam	Cat# ab23707; RRID: AB_447627
Anti-PINK1	NeuroMab	Cat# 73-060; RRID: AB_10675457
Anti-PARKIN	Abcam	Cat# ab77924; RRID: AB_1566559
Anti-CDK1	Abcam	Cat# ab18; RRID: AB_2074906
Anti-COQ2	Abcam	Cat# ab89706; RRID: AB_2291932
Anti-COX15	Abcam	Cat# ab126111; RRID: AB_11131198
Anti-DLD	Abcam	Cat# ab124926; RRID: AB_11128986
Anti-DLST	Abcam	Cat# ab110306; RRID: AB_10862702
Anti-DNM1L	Abcam	Cat# ab56788; RRID: AB_941306
Anti-HSD17B10	Abcam	Cat# ab66054; RRID: AB_1139916
Anti-PARK7	Abcam	Cat# ab76008; RRID: AB_1310549
Anti-PDHA1	Abcam	Cat# ab155096
Anti-SDHA	Abcam	Cat# ab139181
Anti-SOAT1	Abcam	Cat# ab53008; RRID: AB_882634
Anti-SOD1	Abcam	Cat# ab79390; RRID: AB_1603741
Anti-14-3-3-ε	Abcam	Cat# ab137854
Anti-MFF	Abcam	Cat# ab81127; RRID: AB_1860496
Anti-GARS	Abcam	Cat# ab42905; RRID: AB_732519
Anti-NDUFV1	Abcam	Cat# ab55535; RRID: AB_944382
Anti-RARS	Abcam	Cat# ab31537; RRID: AB_2238069
Anti-CKB	Abcam	Cat# ab38211; RRID: AB_731614
Anti-EEF2	Abcam	Cat# ab40812; RRID: AB_732082
Anti-SPTAN1	Abcam	Cat# ab133342
Anti-PRDX6	Abcam	Cat# ab59543; RRID: AB_944762
Anti-PRDX5	Abcam	Cat# ab16944; RRID: AB_2168508
Anti-GSN	Abcam	Cat# ab75832; RRID: AB_1310261
Anti-EIF4G (D-20)	Santa Cruz	Cat# sc-9602; RRID: AB_2095752
Anti-Plectin (C-20, PLEC)	Santa Cruz	Cat# sc-7572; RRID: AB_654218
Anti-Golgin-160 (GOLGA3)	Santa Cruz	Cat# sc-79966; RRID: AB_2113038
Anti-URE-B1 (H-300, HUWE1)	Santa Cruz	Cat# sc-134821; RRID: AB_10646955
Anti-HDGFRP2 (G-19)	Santa Cruz	Cat# sc-55223; RRID: AB_10649523
Anti- IκBε (G-4)	Santa Cruz	Cat# sc-7275; RRID: AB_627774
Anti-Ubiquitin (P4D1)	Santa Cruz	Cat# sc-8017; RRID: AB_628423
Anti-Phosphoserine antibody	Antibodies Online	Cat# ABIN361725; RRID: AB_10787893
Alexa Fluor® 488 anti-rabbit	Abcam	Cat# ab150077; RRID: AB_2630356
Alexa Fluor® 647 anti-mouse	Abcam	Cat# ab150115; RRID: AB_2687948
Bacterial and Virus Strains		
DH5α competent cells	Thermo Fisher	Cat# 18255017
NEB competent *E. coli*	New England Biolabs	Cat# C3040

(*Continued on next page*)

Continued

REAGENT or RESOURCE	SOURCE	IDENTIFIER
Biological Samples		
Mutant PARK2 fibroblasts; subject 1 (code: F-PK1503)	C. Besta, IRCCS Foundation Neurological Institute	Female with familiar PD; compound heterozygous mutations c.823C>T (p.Arg275Trp) and deletion exon 1; age at biopsy-74 (June 2013)
Mutant PARK2 fibroblasts; subject 2 (code: F-DYT396)	C. Besta, IRCCS Foundation Neurological Institute	Female with early-onset PD; compound heterozygous mutations duplication exon 2 and deletion exons 3-4-5; age at biopsy-18 (May 2004)
Mutant PARK2 fibroblasts; subject 3 (code: F-PK589)	C. Besta, IRCCS Foundation Neurological Institute	Male with familiar PD; homozygous mutation c.101_102delAG (p.Gln34Arg*5); age at biopsy-52 (Feb 2009)
Mutant PINK1 fibroblasts; subject 1 (code: F-PK386)	C. Besta, IRCCS Foundation Neurological Institute	Male with early-onset PD; homozygous mutation for c.502G>C (p.Ala168Pro); age at biopsy-59 (June 2003)
Control fibroblasts; subject 1 (code: F-CT01)	C. Besta, IRCCS Foundation Neurological Institute	Mutation: None; Female; age at biopsy-27; Healthy
Control fibroblasts; subject 2 (code: F-CT02)	C. Besta, IRCCS Foundation Neurological Institute	Mutation: None; Female; age at biopsy-27; Healthy
Control fibroblasts; subject 3 (code: F-CT03)	C. Besta, IRCCS Foundation Neurological Institute	Mutation: None; Male; age at biopsy-33; Healthy
Chemicals, Peptides, and Recombinant Proteins		
Rotenone	Sigma Aldrich	Cat# R8875
CCCP	Sigma Aldrich	Cat# C2759
MG-132	Alfa Aesar	Cat# J63250LB0
DSP	Thermo Fisher	Cat# 22585
DMEM	GE Healthcare	Cat# SH30243.LS
FBS	Thermo Fisher	Cat# 12483020
Penicillin/Streptomycin	Fisher Scientific	Cat# SV30010
Magnetic beads/columns	Miltenyi Biotec	Cat# 130-042-601
Trypsin	Promega	Cat# V5280
JC-1	Thermo Fisher	Cat# T3168
Opti-MEM I	Thermo Fisher	Cat# 31985088
Lipofectamine LTX	Thermo Fisher	Cat# 15338100
Brain-derived neurotrophic factor	Thermo Fisher	Cat# 14-8366-62
Retinoic acid	Sigma-Aldrich	Cat# R2625
Hexadimethrine bromide	Sigma-Aldrich	Cat# H9268
Digitonin	GoldBio	Cat# D-180-2.5
Protease/phosphatase inhibitors	EMD Millipore	Cat# 539133/524628
Anti-FLAG M2 beads	Sigma	Cat# F3165
TEV protease	Sigma	Cat# T4455
Strep-Tactin-Sepharose beads	IBA-Lifesciences	Cat# 2-1201-010
Protein A/G microbeads	Milteny Biotec GmbH	130-071-001/130-071-101
D-biotin	EMD Millipore	Cat# 2031-1GM
Trypsin gold	Promega	Cat# V5280
DAPI	Sigma Aldrich	Cat# F6057
MitoTracker	Thermo Fisher	Cat# M7512
RPMI-1640 medium	Thermo Fisher	Cat# 11875-093
Flavin adenine di-nucleotide disodium salt hydrate	Sigma	Cat# F6625
DLD	OriGene	Cat# TP300639

(*Continued on next page*)

Continued

REAGENT or RESOURCE	SOURCE	IDENTIFIER
IκBε	OriGene	Cat# TP760703
ABCD1	Dana Farber	Harvard cDNA Clone ID: HsCD00039863
CDK1	Dana Farber	Harvard cDNA Clone ID: HsCD00000236
COQ2	Dana Farber	Harvard cDNA Clone ID: HsCD00041667
COX15	Dana Farber	Harvard cDNA Clone ID: HsCD00039578
CPOX	Dana Farber	Harvard cDNA Clone ID: HsCD00378277
DARS2	Dana Farber	Harvard cDNA Clone ID: HsCD00377181
DLD	Dana Farber	Harvard cDNA Clone ID: HsCD00288118, 454115
DLST	Dana Farber	Harvard cDNA Clone ID: HsCD00383841
DNM1L	Dana Farber	Harvard cDNA Clone ID: HsCD00040506
FXN	Dana Farber	Harvard cDNA Clone ID: HsCD00288561
HSD17B10	Dana Farber	Harvard cDNA Clone ID: HsCD00367726
HTRA2	Dana Farber	Harvard cDNA Clone ID: HsCD00040783
IDE	Dana Farber	Harvard cDNA Clone ID: HsCD00365724
MFN2	Dana Farber	Harvard cDNA Clone ID: HsCD00039867
MSRB2	Dana Farber	Harvard cDNA Clone ID: HsCD00399900
NDUFS4	Dana Farber	Harvard cDNA Clone ID: HsCD00288529
NDUFS7	Dana Farber	Harvard cDNA Clone ID: HsCD00366813
PARK7	Dana Farber	Harvard cDNA Clone ID: HsCD00383508
PDHA1	Dana Farber	Harvard cDNA Clone ID: HsCD00040816
PINK1	Dana Farber	Harvard cDNA Clone ID: HsCD00042332
SDHA	Dana Farber	Harvard cDNA Clone ID: HsCD00377195
SLC9A6	Dana Farber	Harvard cDNA Clone ID: HsCD00377370
SOAT1	Dana Farber	Harvard cDNA Clone ID: HsCD00040765
SOD1	Dana Farber	Harvard cDNA Clone ID: HsCD00366043
SPG7	Dana Farber	Harvard cDNA Clone ID: HsCD00372256
TFAM	Dana Farber	Harvard cDNA Clone ID: HsCD00400013
VDAC1	Dana Farber	Harvard cDNA Clone ID: HsCD00042189
Critical Commercial Assays		
Cellular ROS/superoxide anion detection kits	Abcam	Cat# ab139476
Phospho-NF-κB p65 (Ser536) (93H1) mAb	Cell Signaling	Cat# 3033
E.Z.N.A. gel extraction	Omega Bio	Cat# D2500-01
QIAprep Spin miniprep	Qiagen	Cat# 27104
GeneJET PCR purification	Thermo Fisher	Cat# K0701
SOD colorimetric kit	BioVision	Cat# K335
H_2O_2 colorimetric/ fluorometric kit	BioVision	Cat# K265
Phusion high-fidelity PCR	Thermo Fisher	Cat# F553S
Prestoblue™ reagent	Thermo Fisher	Cat# A13261
Lysosome purification kit	BioVision	Cat# K235
RNA isolation kit	Roche	Cat# 11828665001
iScript cDNA synthesis kit	BioRad	Cat# 1708890
SsoAdvanced universal SYBR green supermix	BioRad	Cat# 1725270
KiCqStart® SYBR® green primers	Sigma Aldrich	Cat# KSPQ12012
Deposited Data		
Protein complexes	CORUM database	PMID: 17965090
Experimental PPIs	PPI network derived from AP/MS	PMIDs: 27499296, 26496610, 28514442
Experimental PPIs	Co-fractionations coupled with MS	PMIDs: 22939629, 26344197

(*Continued on next page*)

Continued

REAGENT or RESOURCE	SOURCE	IDENTIFIER
Protein, localization, and disease ontology ID	MP assignment and localization, GO annotations, Uniprot, disease ontology ID	PMIDs: 25367773, 26093607
ASD candidates from the interaction network	SFARI; AutDB; Simons Simplex collection	https://gene.sfari.org; PMIDs: 19015121, 25961944
Autism-linked defects	MamPhEA	PMID: 20605928
mRNA expression	RNA-seq: SH-SY5Y neuronal cells	PMID: 26949739
mRNA expression	HEK293 cells	PMID: 25613900 , 21139605
mRNA expression	Brain cell types	GEO: GSE52564
mRNA expression	Tissue excised from brain regions	GEO: GSE45878
Transcriptome data of brain development and cortical neurons	BrainSpan data	PMID: 24267887; http://www.brainspan.org/static/download.html
Transcriptome data of brain development and cortical neurons	CORTECON expression atlas	PMID: 24991954
Transcriptome data of brain development and cortical neurons	MeCP2-mediated regulation in cortical neurons	PMID: 24238429
Disease database	OMIM	PMID: 15608251
Disease database	HGMD	PMID: 24077912
Experimental Models: Cell Lines		
HEK293T	ATCC	Cat# CRL-3216
SH-SY5Y	ECACC	Cat# 94030304
Murine N9 microglia	Savaskan Laboratory	http://savaskan.net/
NTera2 cl.D1	ATCC	Cat# CRL-1973
Jurkat, clone E6-1	ATCC	Cat# TIB-152
Experimental Models: Organisms/Strains		
Mus musculus (C57BL/6)	Jackson Laboratory	Cat# 000664
Oligonucleotides		
sgRNA-PRDX5_F	CRISPR KO	TTGGGAATCGACGTCTCAAG
sgRNA-PRDX5_R	CRISPR KO	CTTGAGACGTCGATTCCCAA
sgRNA-SOD1_F	CRISPR KO	CCACCGTGTTTTCTGGATAG
sgRNA-SOD1_R	CRISPR KO	CTATCCAGAAAACACGGTGG
sgRNA-PINK1_F	CRISPR KO	GGGCCCGGATGTCGTCCTGA
sgRNA-PINK1_R	CRISPR KO	TCAGGACGACATCCGGGCCC
sgRNA-PARKIN_F	CRISPR KO	CTCCCATATGGAGCCCTCTG
sgRNA-PARKIN_R	CRISPR KO	CAGAGGGCTCCATATGGGAG
sgRNA-DLD_F	CRISPR KO	CGTTGGTTGTATTCCTTCAA
sgRNA-DLD_R	CRISPR KO	TTGAAGGAATACAACCAACG
outer-SOD1_F	SOD1 mutants	GCTTCGAATTCCATGGCGAC
outer-SOD1_R	SOD1 mutants	GGCCATTCACATCGCCATTC
inner-SOD1E133Δ_F	SOD1 mutants	GGTGGAAATGAAAGTACAAAGACAGG
inner-SOD1E133Δ_R	SOD1 mutants	TCTTTGTACTTTCATTTCCACCTTTGC
inner-SOD1E133K_F	SOD1 mutants	GGTGGAAATAAAGAAAGTACAAAGACAGG
inner-SOD1E133K_R	SOD1 mutants	TGTACTTTCTTTATTTCCACCTTTGCCC
inner-SOD1E133insTT_F	SOD1 mutants	GGTGGAAATGATTAG AAAGTACAAAGACAGG
inner-SOD1E133insTT_R	SOD1 mutants	CTTTGTACTTTCTAATCATTTCCACCTTTGC
SOD1E133insTT_fix_R	E133insTT mutant	GCTTCGGTCGACCCATC ATTTCCACCTTTGCCCAAG
Transfer-SOD1_F	SOD1-WT/SOD1 E133 mutant to pLEX_307	TAAGCATGTACAAGCTCA GATCTCGAGCTCAAGC

(*Continued on next page*)

Continued

REAGENT or RESOURCE	SOURCE	IDENTIFIER
Transfer-SOD1_R	SOD1 WT/SOD1 E133 mutant to pLEX_307	TAAGCAGTCGACTCATTG GGCGATCCCAATTACACC
Outer-PRDX5_F	PRDX5 mutants	AAGACGGTGCAGTGAAGGAG
Outer-PRDX5_R	PRDX5 mutants	GCCAGTCACAAAGGCATCAT
Inner-PRDX5E80K_F	PRDX5 mutants	GGCAAAGCTGTTCAAGGGCAAG
Inner-PRDX5E80K_R	PRDX5 mutants	AGCTTTGCCAGGTTCACCTTG
Inner-PRDX5K83R_F	PRDX5 mutants	TTCAGGGGCAAGAAGGGTGTG
Inner-PRDX5K83R_R	PRDX5 mutants	TGCCCCTGAACAGCTCTGCC
Inner-PRDX5K85R_F	PRDX5 mutants	GCAGGAAGGGTGTGCTGTTTG
Inner-PRDX5K85R_R	PRDX5 mutants	CCTTCCTGCCCTTGAACAGC
Outer-DLD_F	DLD mutants	GGCACCAAAATCAACGGGAC
Outer-DLD_R	DLD mutants	GCTGCCATTGCTCCCTGG
Inner-DLDS456A_F	DLD mutants	CCGACCTTAGCTGAAGCTTTTAGAGAAGC
Inner-DLDS456A_R	DLD mutants	AAAAGCTTCAGCTAAGG TCGGATGTGCATGAC
Recombinant DNA		
pSOD1E133Δ-AcGFP1	This study	Addgene #83419
pSOD1E133K-AcGFP1	This study	Addgene #83442
pSOD1E133insTT-AcGFP1	This study	Addgene #83441
pLEX_307-SOD1WT	This study	Addgene #83444
pLEX_307-SOD1E133Δ	This study	Addgene #83445
pLEX_307-SOD1E133insTT	This study	Addgene #83446
pLEX_307-SOD1E133K	This study	Addgene #83447
pENTR223-PRDX5E80K (in this study)	This study	Addgene #98692
pENTR223-PRDX5K83R (in this study)	This study	Addgene #98693
pENTR223-PRDX5K85R (in this study)	This study	Addgene #98694
pLD-puro-PRDX5WT-CcVA (in this study)	This study	Addgene #98688
pLD-puro-PRDX5E80K-CcVA (in this study)	This study	Addgene #98689
pLD-puro-PRDX5K83R-CcVA (in this study)	This study	Addgene #98690
pLD-puro-PRDX5K85R-CcVA (in this study)	This study	Addgene #98691
pHAGE_DLDS456A-C-FLAG-HA	This study	Addgene #83479
pLD-puro-CcVA	Moffat Laboratory	Addgene #24588
LentiCRISPR v2	Zhang Laboratory	Addgene #52961
pLV-eGFP	Tsoulfas Laboratory	Addgene #36083
pLEX_307	Root Laboratory	Addgene #41392
pF146 pSOD1WTAcGFP1	Fisher Laboratory	Addgene #26407
pF150 pSOD1G93AAcGFP1	Fisher Laboratory	Addgene #26411
pF148 pSOD1G37RAcGFP1	Fisher Laboratory	Addgene #26409
pF149 pSOD1G85RAcGFP1	Fisher Laboratory	Addgene #26410
pF147 pSOD1A4VAcGFP1	Fisher Laboratory	Addgene #26408
psPAX2	Trono Laboratory	Addgene #12260
pMD2.G	Trono Laboratory	Addgene #12259
Software and Algorithms		
CRAPome	PMID: 23921808	http://www.crapome.org/
SEQUEST	PMID: 24226387	In house
STATQUEST	PMID: 12644571	In house
MaxQuant ver.1.5.0.0	PMID: 19029910	In house
NSAF Scoring	PMID: 17460794	STAR Methods
GO semantic similarity	R package	PMID: 20179076

(*Continued on next page*)

Continued

REAGENT or RESOURCE	SOURCE	IDENTIFIER
CoreMethod	MATLAB code	PMID: 19193141
ClusterONE	Cytoscape app	PMID: 22426491
Gene Set Enrichment Analysis (GSEA)	GSEA software	PMID: 16199517
Hypergeometric test	R function	Stats: R package
Fishers exact test	R function	Stats: R package
Mann-Whitney-Wilcoxon test	R function	Stats: R package
Student's t-test	R function	Stats: R package
Poisson distribution	R function	Stats: R package
Network visualization	Cytoscape ver. 3.3.0	PMID: 25580224
Band signal quantification	ImageJ plugin version 1.51n	PMIDs: 26153368, 22743772
ZDOCK	PMIDs: 12784371, 24532726	Protein docking program
NACCESS	PMID: 5551392	Haiyuan Lab
MATLAB R2012a	MathWorks, Inc	http://www.mathworks.com
Other		
Proteomics data deposition	PRIDE	Accession No: PXD006690

CONTACT FOR REAGENT AND RESOURCE SHARING

Further information and requests for resources and reagents should be directed to the lead contact corresponding author, Dr. Mohan Babu, by email at mohan.babu@uregina.ca.

EXPERIMENTAL MODEL AND SUBJECT DETAILS

Cell Culture and Differentiation

HEK293 or 293T, mouse N9 microglial, and human NTera2 or SH-SY5Y cells used in this study were grown in standard high-glucose Dulbecco's modified Eagle medium (DMEM) containing 4 mM L-glutamine, 1 mM sodium pyruvate, 10% fetal bovine serum (FBS), penicillin (100 U/mL) and streptomycin (100 μg/mL). All cell lines were cultured under standard conditions (37 °C, 5% CO_2). The cells were harvested or passaged when 80% confluence was reached. Passaging of cells was carried out by washing in ice-cold phosphate buffered saline (PBS), followed by the addition of 0.05% Trypsin and 2 mM EDTA and incubation at 37 °C for 10 min, except N9 cells which were scraped and resuspended in FBS-free DMEM. Dissociated cells were collected by gently pipetting and the trypsinization was stopped using DMEM with 10% FBS.

SH-SY5Y cells were differentiated into neuron-like cells by plating the cells at 10,000 cells/cm^2 in DMEM medium containing 10 μM all-trans retinoic acid (Sigma-Aldrich), and changing the medium daily for five days. From day 6 and for 6 additional days, medium was switched to FBS-free DMEM medium containing brain-derived neurotrophic factor (50 ng/mL) and changed every alternate day. Morphological differentiation of SH-SY5Y neural cells and neurite outgrowth was monitored using an EVOS cell imaging system (Invitrogen).

NTera2 cells were seeded in 150 mm tissue-culture dish (2.8 x 10^7 million cells) at high density in DMEM medium. At 80% confluence, cells were scrapped and split no more than 1:4 ratio to avoid premature differentiation. During differentiation, cells were plated at a density of 1 x 10^4 cells/cm^2 and replaced the medium daily with the freshly prepared retinoic acid (10 μM). After two weeks, neuronal differentiation was confirmed microscopically, and cells were harvested and processed for IP/MS.

Human Skin Fibroblasts Cell Culture

Human skin biopsies from PD patients harboring the *PINK1* or *PARKIN* mutations or healthy controls were obtained after signing an informed consent approved by the ethics committee of the IRCCS Foundation Neurological Institute 'C. Besta', Italy. Skin fibroblasts grown following the protocol described by us previously (Zanellati et al., 2015). Briefly, cells were grown in Ham's F14 medium (Euroclone) supplemented with 10% FBS, 4% L-glutamine, 2% penicillin/streptomycin, 1.5% glucose, 1% insulin, 0.1% fibroblast growth factor, and 0.1% epidermal growth factor. Prior to the experiment, the growth medium was changed to Eagle's minimum essential medium (Euroclone) supplemented with 10% FBS, 4% L-glutamine, and 2% penicillin/streptomycin. Human skin fibroblast cells used in our experiments were at passages 8-12. Phenotypic or genotypic data of the PD patients (with *PINK1* and *PARKIN* mutations) and healthy controls are summarized in Table S6 and Key Resources Table.

Preparation of Mouse Brain Lysates

Mice were housed in a pathogen-free laboratory animal care-certified barrier facility. All procedures were approved by the President's Committee for Animal Care at the University of Regina and ensuring compliance with institutional and Canadian Council on Animal Care standards. Briefly, adult C57BL/6 mice were euthanized by cervical dislocation and their brains were quickly removed and washed twice with ice-cold PBS containing a 1X protease inhibitor cocktail (Sigma-Aldrich) and flash-frozen in liquid nitrogen for future use. The brains were homogenized in RIPA (Radio-IP assay) buffer containing a 1X protease inhibitor cocktail with 10 strokes of a mechanical pre-chilled Dounce glass tissue homogenizer. The homogenate was centrifuged at 3,000 *xg* for 10 min at 4°C, and the supernatant was used for immunoblotting.

METHOD DETAILS

Target MP Selection

Proteomics screens were carried out by targeting 27 nuclear-encoded human MPs linked with NDs as supported by database annotations, peer-reviewed literature, or a hand-picked set of well-established and widely used subcellular localization databases (Table S1). Information on mt localization was retrieved from the recent literature-compiled census of human MPs (Calvo et al., 2016; Malty et al., 2015). Disease links for genes encoding PPI pairs were retrieved from the GWAS, OMIM, and HGMD databases. Since OMIM provides only gene-disease associations, each gene encoding the binding protein was mapped to a Uniprot identifier and OMIM disease association to its respective disease ontology ID and parent disease categories.

Gateway Cloning

Gateway cloning-compatible plasmids (pDONR221/223 or pENTR223) encoding cDNAs of the select set of MPs from the human ORFeome collection were obtained and sequence verified at Dana Farber/Harvard Cancer Center DNA Resource Core (clone IDs provided in Table S6). Each target MP was in-frame with a Gateway cassette containing the triple VA-purification tag (3×FLAG, 6×HIS, and 2×STREP epitopes; FLAG and HIS separated by the dual tobacco etch virus (TEV) protease cleavage sites) at the C-terminus.

Briefly, ~50 ng of the Gateway-compatible human cDNA-encoding plasmid was combined with 100 ng of the destination vector (pLD-puro-CcVA) and 1 μL of the Gateway cloning LR II enzyme mix (Thermo Fisher Scientific) into a final volume of 10 μL with TE buffer (pH 8.0). The enzymatic reaction was incubated at 25 °C for 2 h, and 1 μL of proteinase K was added to the mix and incubated at 37 °C for 10 min. One μL of the resulting mixture was incubated with 50 μL of One Shot Stbl3 chemically competent *Escherichia coli* (Thermo Fisher Scientific) on ice for 30 min, followed by heat shock at 42 °C for 45 sec and incubation on ice for 2 min. Two hundred μL of SOC medium was added to each transformation mixture and tubes were shaken at 30 °C for 1 h and then plated on freshly-prepared agar plates containing 100 μg/ml ampicillin, and incubated in a moisture-saturated incubator at 30 °C overnight.

The following day, colonies were picked and grown in Luria-Bertani (LB) medium containing freshly prepared ampicillin (100 μg/mL). Cloned plasmids were extracted from the culture and then sequence confirmed by Sanger sequencing using two independent, U6-forward and CMV-forward primers, at the TCAG (The Centre for Applied Genomics) DNA sequencing facility (Hospital for Sick Children, Toronto, Canada).

Stable Cell Line Generation

Lentiviral particles carrying the VA-tagged MP cDNAs were generated according to protocols provided by The RNAi Consortium (Broad Institute of MIT and Harvard). Briefly, 7.5 μg of the lentiviral expression vector encoding VA-tagged MP cDNA was mixed with 7.5 μg psPAX2 (packaging plasmid), 0.75 μg pMD2.G (envelope expressing plasmid), and 8.25 μL of the PLUS reagent provided with Lipofectamine LTX into a total volume of 750 μL with Opti-MEM I (Minimal Essential Medium) reduced serum medium. In another sterile tube, 52.5 μL Lipofectamine LTX was mixed with 697.5 μL Opti-MEM I medium. Both mixtures were combined and incubated at room temperature for 15 min.

The transfection mixture added to HEK293T cells at ~40% confluence in 100 mm cell culture dishes was incubated at 37 °C in 5% CO_2 with complete DMEM without antibiotics. After 6 hrs, the medium was replaced with DMEM containing penicillin (100 U/mL) and streptomycin (100 μg/mL) and the lentiviral particles collected 24 and 48 h post-transfection were filtered through a low protein-binding poly-ethersulfone syringe filter (0.4 μm). Finally, HEK293 cells at ~6.25% confluence were transduced with lentiviral supernatant at 0.3-0.5 multiplicity of infection (MOI) for 2 days along with filter-sterilized (0.22 μm syringe filter) hexadimethrine bromide (10 μg/mL) to enhance lentiviral infection, followed by 3 days of puromycin (2 μg/mL) selection to ensure effective isolation of stable cells, expressing the introduced VA-tag MP. After confirming the VA-tag by immunoblotting using anti-FLAG Ab, the stable transformants were expanded in five 150 mm plates to 80% confluency (9 x 10^7 cells), and cells were harvested in 3 batches of 5 plates each, representing 3 biological replicates. The cell pellets were either processed immediately or stored at -80 °C for future use.

Determining MOI

Media containing lentivirus was combined with filter-sterilized hexadimethrine bromide (10 mg/mL) to a final concentration of 10 μg/mL. Serially diluted lentiviral supernatant was added to HEK293 cells and seeded in 24-well plates at ~6.25% confluence (1.6 x 10^3 cells/well). After 24 h of incubation, the viral media was replaced with fresh DMEM and cells were subjected to puromycin (2 μg/mL) selection for 3 days. Cell viability was measured in puromycin-selected HEK293 cells using Prestoblue™ cell viability

reagent according to manufacturer's instructions. Briefly, 1 part of PrestoBlue reagent was mixed with 9 parts of DMEM medium and incubated with lentivirus-transduced HEK293 cells at 37 °C for 2 h prior to absorbance reading at 570 nm and 600 nm (as reference) using an Epoch microplate reader (BioTek). Percent survival was quantified by averaging at least 3 biological and 25 technical replicates, deconvoluted to 0.3-0.5 MOI using a Poisson distribution, where the probability of a cell being infected by a lentiviral particle corresponded to 26-39% cell survival. This MOI ensured relatively low levels of expression of the FLAG-tagged MPs, minimizing the disruption of cellular protein homeostatic mechanisms.

Crosslinking

Stably-transduced (or WT) HEK293 cells expressing VA-tagged MPs, SH-SY5Y neuronal, or mouse N9 cells were crosslinked using the cell membrane-permeable crosslinking reagent DSP (0.5 mM) and incubated at room temperature for 30 min. The crosslinking reaction was quenched by treating the cells with 100 mM Tris-HCl (pH 7.5) and 2 mM EDTA at room temperature for 10 min. Cells were then collected by gentle pipetting, followed by washing (twice) and centrifugation at 1,300 *xg* for 5 min. DSP solution prepared at 0.25 M in dimethyl sulfoxide was diluted in PBS to a 0.5 mM final concentration.

Cytosolic, Mt, and Lysosomal Isolation

Mt were isolated from HEK293 cells expressing VA-tagged MPs and SH-SY5Y or N9 cells using the following procedure. Briefly, crosslinked cells from 2 to 5 x 150 mm tissue-culture dishes, depending on the cell types, were harvested and washed twice in ice-cold PBS. Cells were then resuspended in 1.1 mL of ice-cold buffer containing 10 mM NaCl, 1.5 mM $MgCl_2$ and 10 mM Tris-HCl (pH 7.5), and allowed to swell for 10 min, followed by several repeated passages through a syringe fitted with a 22-gauge needle or with a pre-chilled Dounce glass tissue homogenizer. The lysed cells were added to 800 μL of ice-cold buffer (210 mM mannitol, 70 mM sucrose, 5 mM Tris-HCl (pH 7.5) and 1 mM EDTA) and centrifuged at 1,300 *xg* for 5 min at 4 °C. The resulting supernatant was centrifuged further at 17,000 *xg* for 15 min at 4 °C, where the cytosolic (supernatant) and mt (pellet) fractions were separated and used for affinity purification or immunoblotting as described below. Likewise, lysosome from the cultured cells of choice was fractionated, following the manufacturers isolation procedure (BioVision).

AP/MS and IP/MS Screens

The fresh (or frozen) mt pellets isolated from the crosslinked HEK293 cells expressing VA-tagged MPs were resuspended with buffer containing 30 mM Tris-HCl (pH 7.5), 150 mM NaCl, 1% digitonin, and supplemented with protease and phosphatase inhibitors. Cell lysates were incubated in this buffer on ice for 30 min, then centrifuged at 23,000 *xg* for 20 min at 4 °C. The harvested supernatant was incubated with 100 μL of anti-FLAG M2 agarose beads at 4 °C for 4 h with gentle rotation. Supernatant with beads was transferred to Bio-spin disposable chromatography columns and washed four times with 1 mL ice-cold buffer (50 mM Tris (pH 7.6) and 150 mM NaCl) with 10 min wait in between washes.

In the case of Strep-Tactin-FLAG purifications, 100 μL TEV buffer (10 mM Tris-HCl (pH 7.9), 125 mM NaCl, and 0.1% digitonin), 5 μL TEV protease (2 mg/mL), and 2 μL 3×FLAG peptide (5 mg/mL) were added to the FLAG-IPs and rotated overnight at 4 °C. The following day, 20 μL Strep-Tactin-Sepharose bead (IBA) slurry was washed three times with 1 mL TEV buffer and added to the TEV eluents. The mixture was incubated for 4 h at 4 °C. The column was washed 4 times with TEV buffer (with 10 min wait in between), followed by elution with 50 mM ammonium bicarbonate and/or 2 mM D-biotin (Sigma). The eluted samples were dried using a Savant Speedvac prior to processing in MS.

To perform the pulldown experiments with endogenous proteins, we considered an Ab to be appropriate as long as: (i) it was raised in rabbit and is polyclonal, (ii) the bait MP IPed with the Ab of interest is recovered from MS, and (iii) antibodypedia or commercial vendors (e.g. Abcam) have recommended it for IP. Briefly, IP with primary Ab was performed by harvesting the crosslinked mouse brain, HEK293, and SH-SY5Y (5 x 150 mm tissue-culture dishes; 1.4 x 10^7 cells/dish) or NTera2 (2 x 150 mm dishes; 2.8 x 10^7 cells/dish) neuronal cells at ~80% confluency and pelleted via centrifugation at 1,300 *xg* for 5 min. The pelleted cells were lysed in RIPA buffer (150 mM NaCl, 50 mM Tris-HCl (pH 7.5), 0.1% sodium dodecyl sulfate, 1% Na deoxycholate, 1% NP-40, and 1mM EDTA), followed by 10-20 strokes with a pre-chilled glass Dounce homogenizer and centrifugation at 14,000 *xg* for 20 min at 4 °C to remove insoluble debris. After measuring the protein concentration using a Bradford assay, ~10 mg protein was incubated with 3 μg protein-specific Ab for 1 h at 4 °C with gentle rotation. To this mixture, 100 μL μMACS protein A or G magnetic microbeads was added and incubated at 4 °C for an additional 4 hrs with gentle rotation. The resulting sample mixture was purified by magnetic columns, washed three times using RIPA buffer containing detergent, followed by two washes with detergent-free buffer.

The Speedvac dried samples were diluted with 50 μL digestion buffer (50 mM NH_4HCO_3 and 1 mM $CaCl_2$) and incubated with 0.9 μL of 2 mM TCEP-HCl (Tris (2-carboxyethyl) phosphine) at room temperature for 45 min to reduce protein disulfide bonds. To this mixture, 1 μL of 10 mM iodoacetamide alkylating agent was added and incubated in the dark for 40 min, prior to digesting the mixture with trypsin gold (Promega). The trypsinized samples were incubated overnight at room temperature by mixing gently using a rocking shaker. The reaction was stopped by adding 1 μL of acetic acid. The digested samples were processed using the following steps: first, a zip tip was equilibrated by aspirating 10 μL of wetting solution (70% acetonitrile in 0.1% formic acid) and dispensing to waste three times, then washed with 100% HPLC grade H_2O in 0.1% formic acid by aspirating and dispensing 10 times, and finally washed three times with wetting solution and dispensed. After washing, 10 μL of digested sample was aspirated and dispensed twice and then air-dried and resuspended in 20 μL of 0.1% formic acid.

Chromatographic separation of peptides was performed on an EASY-nano high-performance liquid chromatography 1000 (Proxeon), where samples are injected onto a nano C18 column (10 cm x 75 μm ID, 3 μm, 100 Å) employing a water/acetonitrile/0.1% formic acid gradient for 100 min at a flow rate of 0.30 μl/min. Peptides were separated using 1% acetonitrile and increased gradually to 3% acetonitrile in the first 2 min and then a linear gradient from 3 to 24 % of acetonitrile for 74 min, followed by a gradient from 24 to 100 % acetonitrile for 14 min and a 10 min wash with 100 % acetonitrile. Eluted peptides were directly sprayed into the Orbitrap Elite mass spectrometer (Thermo Fisher Scientific) using positive electrospray ionization at an ion source temperature of 250 °C and an ionspray voltage of 2.1 kV.

Full-scan MS spectra (m/z 350–2000) were acquired in the Orbitrap at mass resolution of 60,000 (m/z 400). The automatic gain control settings were 1e6 for full FTMS scans and 5e4 for MS/MS scans. Fragmentation was performed with collision-induced dissociation (CID) in the linear ion trap when ion intensity reached >1,500 counts. The 15 most intense ions were isolated for ion trap CID with charge states $\geq$ 2 and sequentially isolated for fragmentation using the normalized collision energy set at 35%, activation Q at 0.250 and an activation time of 10 ms. Ions selected for MS/MS were dynamically excluded for 30 s.

Immunoblotting

Immunoblotting was performed using a standard protocol. Briefly, samples were eluted in Laemmli buffer and separated on 10% SDS-PAGE gel, and transferring to PVDF (Polyvinylidene difluoride) membranes using an iBlot™ transfer system (Thermo Fisher Scientific). PVDF membranes were blocked in 5% dry fat-free milk in TBST (Tris Buffered Saline with Tween 20) and blotted with appropriate primary Ab for 1 h at room temperature or overnight at 4 °C in 2% dry fat-free milk in TBST. Membranes were washed twice in TBST at room temperature and incubated with appropriate HRP-conjugated secondary Ab for 1 h in 2% dry fat-free milk in TBST and washed three times in TBST. Immunoreactive proteins were detected by chemiluminescence (Thermo Fisher Scientific) and imaged using a molecular imaging station (Kodak ISM 2000MM). The digitalized immunoblot bands were quantified by measuring band pixel using an automated ImageJ plugin, and the total measured pixels of each band were normalized to the corresponding loading control.

Immunofluorescence

Acid-washed ''squeaky clean'' glass coverslips (No 1.0, Ted Pella) were prepared by ultrasonicating the coverslips in water, with and without detergent, for 30 min, followed by heating at 60 °C in 1N HCl overnight, washing with deionized water, and ultrasonicating in 70% and 95% ethanol for 15 min twice. These coverslips were stored in 95% ethanol at room temperature and washed with ice-cold PBS five times, and then coated with 10 μg/mL fibronectin (Corning) prior to the seeding of HEK293 cells stably expressing VA-tagged MPs (or WT) at 25% confluence. After 24 h of incubation at 37 °C in a 5% CO_2 humidity-saturated incubator, the coverslips with cells were washed with PBS twice, followed by 3% para-formaldehyde fixing for 15 min at room temperature, washing three times with PBS, and permeabilizing with 0.25% Triton X-100 in PBS for 10 min, and washing three times with PBS.

Next, coverslips with cells were blocked in 10% FBS solution in PBST (0.1% Tween 20 in PBS) containing 0.3 M glycine for 30 min at room temperature. After removing the blocking solution, the cells were incubated with primary Ab (anti-FLAG or Abs raised against MPs; 1:100 dilution; see Table S6) overnight at 4 °C in a humidity-saturated incubator then washed three times with ice-cold PBS. Coverslips with cells were incubated with Alexa Fluor® 488 anti-rabbit or Alexa Fluor® 647 anti-mouse secondary Abs (1:200 dilution) for 1 h at room temperature. The cells were then washed three times with ice-cold PBS and twice with ice-cold water prior to mounting in Fluoroshield plus DAPI (Sigma Aldrich) medium. After sealing the coverslips with clear nail polish, the co-localized proteins were examined with a Zeiss Observer Z1 inverted microscope with Colibri 2 epifluorescence at an appropriate wavelength.

To visualize proteins localized in the mt, the stably expressed VA-tagged MPs in HEK293 cells were seeded onto glass coverslips and labeled with 100 nM red-fluorescent mt marker (MitoTracker Red CMXRos) for 30 min at 37 °C in a 5% CO_2 incubator.

Validating mtPPIs by PCP BN-PAGE

While this manuscript was in preparation, a parallel study (Scott et al., 2017) was conducted by the group of Leonard Foster (University of British Columbia), monitoring changes during the initiation of apoptosis in both mt membrane and cytoplasmic complexes in response to the Fas mediated apoptotic cascade in Jurkat T-cells. This was done using PCP (Protein Correlation Profiling) by stable isotope labeling with amino acids in cell culture (SILAC) coupled with MS. Detailed experimental procedures, including mt preparations from Jurkat cells, SILAC labeling, BN-PAGE, and MS was carried out essentially as described (Scott et al., 2017). Using this approach, we captured 4 interactions (HSD17B10-EEF2; HSD17B10-TRAP1; VDAC1-VDAC2; and HSD17B10- PTBP1) in our FLAG MP network (while 13 overlapping PPIs failed to meet our stringent filtering criteria). PCP profiles are shown for the 3 PPI pairs in Figure S2F.

Generation of KO Cells

Oligonucleotide pairs encoding 20-nt guide RNAs (sgRNAs) targeting sequence for genes encoding interacting proteins were designed using standard procedure. Briefly, 1 μL of the reconstituted forward and reverse strands of oligos (100 μM) for each sgRNA template (Sigma-Aldrich) was combined with 1 μL T4 DNA ligase buffer (NEB) and 0.5 μL T4 polynucleotide kinase (NEB) and nuclease-free water to a final volume of 10 μL. The mixture was incubated at 37 °C for 30 min, heated to 95 °C for 5 min, and ramped down to 22 °C at a rate of 6 °C/min.

LentiCRISPR-v2 digested with FastDigest Esp3I and dephosphorylated with FastAP thermosensitive alkaline phosphatase according to manufacturer's instructions (Thermo Fisher Scientific) was run on a 1% agarose gel. The DNA band corresponding to the large fragment of the plasmid (i.e. the plasmid backbone) was extracted from the agarose gel using an E.Z.N.A. gel extraction kit (Omega Bio-tek). The annealed and phosphorylated sgRNA-encoding oligonucleotide was diluted (1:200) and 1 μL of the dilution was combined with 50 ng of the dephosphorylated lentiCRISPR-v2 backbone, 1 μL T4 DNA ligase buffer, and 1 μL T4 DNA ligase (NEB) and nuclease-free water to a total volume of 10 μL. After incubating at room temperature for 10 min, 1 μL of the mixture was added to 50 μL of chemically competent Stbl3 *E. coli* cells and transformed as described above. Colonies picked were grown in LB medium containing ampicillin (100 μg/mL) and plasmid DNA extracted using QIAprep Spin Miniprep Kit (Qiagen). Resulting DNA was sequence verified at the TCAG DNA sequencing facility to confirm correct insertion of sgRNAs using a universal U6-forward primer.

SH-SY5Y neuronal cells (~6 x 10^5 cells per 100 mm dish) were next transiently transfected with ~15 μg of sequence-verified plasmid DNA, 15 μL PLUS reagent and Opti-MEM I reduced-serum medium in a total volume of 750 μL. To this mix, 60 μL Lipofectamine LTX and 690 μL Opti-MEM I was added and incubated at room temperature for 15 min prior to combination with the SH-SY5Y neuronal cells. Two days post-transfection, cells were selected using puromycin (2 μg/mL) for 3 days, and further expanded and processed for immunoblotting to confirm gene KO. In the case of N9 cells, lentiviral production and stable cell line generation described above was adapted to generate KOs of *PINK1*, *PARKIN* or *DLD* using CRISPR-Cas9.

Mutagenesis

Human *SOD1*, *PRDX5*, or *DLD* variants were generated by designing two different sets of primers in each case, outer and inner primers (sequences shown in Table S6). Outer primers were designed using the Primer3Plus software, flanking the region where mutations and suitable restriction sites are located. Inner primers with the desired mutations, annealing at the proper region in the plasmids encoding SOD1, PRDX5, or DLD cDNAs were designed manually. Three rounds of PCR reactions were employed for every mutation. Briefly, two first-round PCR reactions were carried out using forward outer and reverse inner primers or forward inner and reverse outer primers. The amplicons were purified using a GeneJET PCR purification kit. Next a second PCR reaction was carried out by combining equimolar amounts of both first PCR products and using an overlap extension PCR without outer primers. The resulting amplicons were purified and used as template for the third PCR reaction with outer primers to maximize the PCR product yield containing the desired mutation.

The plasmid encoding SOD1, PRDX5, or DLD and the third PCR amplicon containing the desired mutation were restriction-digested using appropriate enzymes, gel purified, mixed, and ligated as described above. One μL of the ligation reaction mixture was then transformed in chemically competent bacteria, grown overnight, and colonies were picked and expanded in LB media with appropriate antibiotic. In the case of *SOD1*-E133insTT variant, a TT after the second nucleotide of E133 codon was inserted (changing the nucleotide sequence from GAAGAA> GATTAG) to create a premature STOP codon, which was removed by PCR-cloning while keeping the GFP-tagging intact. The plasmid DNA of the *SOD1*, *PRDX5*, or *DLD* variants were then extracted and sequence verified in TCAG using CMV or EF-1α forward primers. All plasmids used in this study have been deposited in Addgene.

Structural Modeling

To analyze the interface residues of SOD1-PRDX5 interaction, we employed a template-free (molecular docking) strategy that relies on physics-based calculations to produce low-energy conformations between molecular subunits with known structures. Using the docking program, ZDOCK, we produced 2,000 structural conformations between two PDB chains corresponding to SOD1 and PRDX5 (4B3E and 4K7O, respectively). For the highest scoring docked structure, we determined residues at the complex interface using NACCESS to measure the change in solvent accessible surface area between bound and unbound states of this complex. Residues with a minimum 15% solvent accessible surface area in the unbound state whose absolute solvent accessible surface area changes decreased by ≥1.0Å squared were considered to be at the interface of the bound structure. This suggested interface residues for SOD1 were at positions 71, 132, 133, 134, 136, 137, and 138, and PRDX5 at 80, 83, 84, 85, and 187. By intersecting the interface residues of both SOD1 and PRDX5, we were able to identify two (133 and 134) residues of interest in SOD1, whose mutations have been linked to ALS (Saccon et al., 2013)

Cellular, NF-κB, and Proteolytic Assays

Intracellular H_2O_2, SOD, and succinate or lactate dehydrogenase activities were measured following the instructions from commercial kits (BioVision), while $O_2^{\bullet -}$ or ROS accumulations were determined using cellular ROS/$O_2^{\bullet -}$ detection kits (Abcam), and mt membrane potential by MitoProbe JC-1 assay kit (Thermo Fisher Scientific). Fluorescence levels were measured with a microplate reader (Synergy HTX) or visualized using a Zeiss Observer Z1 inverted microscope with Colibri 2 epifluorescence.

The phosphorylation of NF-κB p65 level was measured in nuclear fraction as previously described (Rosner et al., 2013). The mouse N9 cells expressing control and *PINK*, *PARKIN* or *DLD* KOs, grown in 100 mm tissue culture dishes at 6 x 10^6 cells/dish were treated with kinetin (25 μM; the precursor of the ATP analog kinetin triphosphate) or adenine (25 μM) at indicated time points (Figure 7G) and/or with respiratory inhibitors (3 μM CCCP or rotenone) for 1 hr, washed twice in ice-cold PBS, and centrifuged at 200 *x* g for 10 min. After discarding the supernatant, the cells were resuspended in 300 μl of buffer containing 20 mM Tris-HCl (pH 7.6), 0.1 mM EDTA, 2 mM $MgCl_2$, 0.5 mM NaCl, 0.5 mM Na_3VO_4, and 2X phosphatase inhibitor cocktail. Cells were incubated at room temperature for 10 min on ice and then mixed gently with 30 μl of 10% Nonidet P-40 for the cells to lyse membrane in hypotonic

medium. The cell suspension was passed in 27G syringe needle, followed by harvesting the nuclei by centrifugation at 500 *x* g for 3 min. The nuclear pellet resuspended in the lysis buffer (20 mM Tris-HCl (pH 7.6), 150 mM NaCl, 1 mM EDTA, 1 mM EGTA, 1% (v/v) Triton X-100, 2 mM sodium pyrophosphate, 1mM β-glycerophosphate and 1mM Na_3VO_4) was centrifuged at 13,000 *x g* for 10 min. The resulting supernatant was used to measure Ser536 NF-κB p65 activity as per the manufacturer's protocol (Cell Signaling) at 450 nm with Epoch microplate absorbance reader. The nuclear protein concentration was determined using the Bradford assay.

The proteolytic assay was carried out as previously described (Babady et al., 2007) with few modifications. Briefly, 293T cells were infected with lentiviral particles expressing C-terminal, tandem affinity purification (TAP) tag fusion of a proteolytically inactive S456A *DLD* variant or WT DLD, followed by puromycin selection. While TAP-tag consists of two adjacent affinity purification tags (FLAG and HA), we used anti-HA Ab to purify WT or mutant DLD from 20 x 150 mm tissue-culture dishes (3.6 x 10^8 million cells per dish at ~80% confluency). Cells were washed twice with PBS, and the resulting pellet resuspended in 10 ml Buffer A (100 mM Tris-HCl, pH 8.0; 150 mM NaCl; 1 mM EDTA, pH 8.0) was sonicated for 15 s with 15 s cooling cycles for 3 min on ice. Cell-debris was pelleted at 12,000 *x* g at 4 °C for 15 min. Anti-HA Ab was added to the 10 ml cell-free extract and incubated at 4°C for 1 h, followed by the addition of 1 ml μMACS Protein A microbeads and 3 hrs incubation with shaking at 4°C. One ml of the lysate-resin mixture was loaded into 10 multi-8 columns with MultiMACS Separation Unit. Columns were washed 5 times with 1 ml Buffer A, and eluted with 100 μl of elution buffer (8 M urea, 5 mM DTT in Buffer A). Accumulated elution's (1 ml) were dialyzed against 10 μM flavin adenine dinucleotide and 10 mM DTT in Buffer A for 24 hrs at 4°C with continuous stirring. The refolding mixture was again dialyzed 3 times for 4 hrs with Buffer A at 4°C using a dialysis tube with 3.5 kDa MWCO for purifying the sample.

The proteolytic reaction of purified WT or catalytic mutant (S456A) of DLD was analyzed by silver staining. Each reaction contained 1 μg DLD (OriGene), 0.2 μg DLD WT or catalytic mutant (DLDS456A), and 2 μg IκBε (OriGene) in 100 μl of 10 mM Tris-HCl (pH 8.0) and 50 mM NaCl. IκBε cleavage products by DLD was assessed after incubating the samples for 2 hrs at 37°C and analyzed by silver staining and MS. To assign protein corresponding to the band observed in silver stain gel, the select cut bands were trypsinized using standard MS procedures. The resulting tryptic peptides were analyzed by Orbitrap-Elite coupled with Easy nLC system.

Quantitative Real-Time PCR

The mouse N9 cells stably expressing the control and PINK1, PARKIN or DLD sgRNAs were grown in 6-well plates at about 1x10^6 cells/well, incubated overnight in FBS-free medium, and then exposed to vehicle or rotenone. After 5 hrs, cells washed with ice-cold PBS twice were lysed using lysis buffer supplied in the total RNA extraction kit (Roche). Standard cDNA reaction was carried out from 0.5 μg total RNA extracted from the harvested cells according to the manufacturer's instructions using iSCRIPT cDNA synthesis kit (BioRad). Predesigned KiCqStart® SYBR® Green Primers (Sigma) for murine β-actin (reference control to normalize expression levels) and interleukin 1β were used to detect cDNA level corresponding to each gene using SsoAdvanced Universal SYBR Green Supermix (BioRad). SYBR green fluorescence was measured by Eppendorf Mastercycler® ep realplex4 Gradient S under standard thermal cycling protocol, and fold changes relative to control vehicle was determined by the 2-ΔΔCT procedure.

QUANTIFICATION AND STATISTICAL ANALYSIS

Protein Identification, NSAF Scoring, and Data Filtering

RAW files from affinity purification or IP combined with MS experiments were converted into mzXML files and high-confidence matches among the resulting MS/MS spectra were mapped against a reference human protein sequences using the SEQUEST database search engine. Matches were evaluated by the STATQUEST probability algorithm. For PCP BN-PAGE experiments, MaxQuant ver.1.5.0.0 was used for identification and quantification, with resulting biological replicates searched to ensure a false discovery rate of less than 1% (Scott et al., 2017).

As network quality depends on the interaction dataset, we employed the NSAF scoring approach to obtain high-quality spectral counts and discriminate non-specific binders from genuine interactors prior to network generation. Briefly, the NSAF was calculated for each interacting bait-prey pair in a purification, taking into account of the number of spectral counts (or peptides) of the prey protein identified by MS, the length of the prey protein, and the total number of peptides for all prey proteins in the bait MP purification:

$$NSAF_{i,j} = \frac{\frac{SC_{i,j}}{L_j}}{\sum_{k=1}^{N} \frac{SC_{i,k}}{L_k}}$$

Where SC_{ij} and L_j are the spectral count and length of the prey protein *j*, respectively, and *N* is the number of all prey proteins in the purification of a bait MP *i*. Since purification for each bait MP was performed more than once, the average *NSAF* score was assigned to the bait-prey pair.

High-quality interactions were notable after eliminating co-purifying proteins at 90% confidence threshold as assigned by STATQUEST, and filtering additionally for: (1) common contaminants (or non-specific binders) from WT control purifications, (2) CRAPome contaminants, (3) interacting protein pairs not present in two-thirds of the biological replicate experiments, (4) proteins that repeatedly co-purified with large numbers of disparate MP bait purifications, and (5) PPI pairs with NSAF values from individual

MP bait purifications that are less than median NSAF values from the control purifications and those not present in HEK293 or SH-SY5Y Ab datasets. Interactions that were retained after these filtering were assembled for cluster generation using coreMethod (Leung et al., 2009) and visualized by Cytoscape.

CoreMethod and Other Bioinformatic Analyses

To identify multiprotein complex assemblies, we partitioned the neuronal-relevant PPIs into distinct sub-networks using the CoreMethod algorithm (Leung et al., 2009), encompassing a core and an attachment. A core subunit is the central member of a cluster, while an attachment is the subunit that interacts with at least half of its complex subunit memberships. While an attachment can be a member of many multiprotein complexes, a subunit of a cluster is designated as core component if they are: highly connected with other proteins, unique within a cluster, and bound by the attachment proteins to form a complex.

The algorithm considers two proteins, *p1* and *p2*, having degrees (i.e. number of PPIs) *d1* and *d2*, respectively, as core members of a complex if the interaction *i* (*i* = 0 or 1) between these two proteins and the number of common neighbors between them *c* is assessed. The probability (*p-value*) of proteins *p1* and *p2* is then computed, having $\geq$ *i* interactions and $\geq$ *c* common neighbors between them under the null hypothesis that degrees *d1* and *d2* are randomly assigned in the PPI network following a uniform distribution. The steps used in the calculation of *p-value* includes probabilities of *p1* and *p2* with: (i) *i* interactions between them and (ii) exactly *c* common neighbors. The product of probabilities obtained from (i) and (ii) were combined to derive a final *p-value*, where a significant small *p-value* suggest *p1* and *p2* as likely core proteins of the same complex. Using this strategy, the predicted complexes are ranked based on the *p-value*, and only clusters with $P \leq 0.05$ were considered as significant and reported in Table S4.

To identify ASD-relevant subnetwork of bait MPs and their interactions, we mapped proteins from the FLAG MP network to various literature sources (Table S5). These included the SFARI (Simons Foundation Autism Research Initiative) Human Gene Module; AutDB, a gene reference resource for autism; and exome sequencing data of ASD patients from the Simons Simplex collection (2,377 families including 1,786 quads and trios, for a total of 8,917 exomes). Using these datasets, we found 46 interacting proteins with disease-associated variants in ASD probands or siblings (Table S5). Nearly a dozen of these ASD-linked binding partners regulated by FMRP and/or MeCP2 (Figure 4E) were retrieved through literature curation.

All bait-prey pairs in the FLAG MP network were analyzed for enrichment of annotations in GO biological processes or PFAM domains using Gene Set Enrichment Analysis. RNA expression data of the human tissues from brain regions and spinal cord (Figure S2C), 206 samples in total (GSM1117145-GSM1117930; GSE45878), were downloaded from the NCBI Gene Expression Omnibus (GEO). Expression values were used to compute the Pearson's correlation between all proteins as well as for the interacting proteins from SH-SY5Y neuronal cells for each brain region. In the case of RNA-seq expression profiles from the BrainSpan data (Parikshak et al., 2013), expression value (FPKM) for each ASD-linked interacting protein, as well as for the corresponding bait MP, were compiled from the cortical development stage listed in Table S5. However, since the data for each stage encompassed expression values from multiple regions of the brain, we computed the average expression value for each protein. Expression values were also averaged when multiple brain developmental stages (e.g. 8-10, 17-21, and 24-26 weeks after conception) were considered.

Statistical Tests

The results presented in this study were achieved with rigor by analyzing the functional or follow-up assays with a minimum of three independent biological and/or technical replicates, unless otherwise stated. Appropriate sample size were chosen based on assays to ensure that we have enough statistical power to draw conclusions. In all our assays, significance was determined using appropriate statistical tests that are of acceptable standard in the field; wherever possible, non-parametric tests, mean ± SD, and number of replicates were outlined in the figure legends.

DATA AND SOFTWARE AVAILABILITY

All raw proteomic data from this work is submitted to the PRIDE repository (Accession: PXD006690) at the European Bioinformatics Institute, in accordance with the data sharing policy. Codes used in generating the results are described above in detail.